# Computational Investigations of Integrated Vortex-Odor Dynamics in the Wake of Fish for Underwater Sensing

by

Maham Kamran

A thesis presented to Lakehead University in fulfilment of the

thesis requirement for the degree of

Master of Science in Mechanical Engineering

Supervisor

Muhammad Saif Ullah Khalid, PhD, P.Eng

Thunder Bay, Ontario, Canada, 2025

I hereby declare that I am the sole author of this thesis.

Maham Kamran

I authorize Lakehead University to lend this thesis to other institutions or individuals for the purpose of scholarly research.

Maham Kamran

I further authorize Lakehead University to reproduce this thesis by photocopying or by other means, in total or in part, at the request of other institutions or individuals for the purpose of scholarly research.

Maham Kamran

Lakehead University requires the signatures of all persons using or photocopying this thesis.

Please sign below and give address and date.

# Abstract

This research investigates the interplay between vortex dynamics and odor transport in undulatory swimming using high-fidelity computational fluid dynamics (CFD) simulations. Building upon initial two-dimensional (2D) analyses, we extend our study to three-dimensional (3D) simulations to quantify odor effectiveness and the role of kinematics and morphology in chemical dispersion. Our results reveal that odor transport is strongly coupled with vortex structures, with convection dominating over diffusion in aquatic environments. Kinematics, rather than body shape, primarily dictate odor transport, with anguilliform swimmers generating broader and more persistent odor trails than carangiform swimmers. Swapping kinematics between Jackfish and Eel models confirms that swimming motion, not morphology, governs odor dispersal. Increasing undulation amplitude enhances odor transport by increasing momentum transfer, reinforcing the dominance of vortex-driven convection. Expanding our study to fish schooling, we analyze odor dispersion across different group configurations. While lateral odor spread intensifies with group size, downstream transport remains largely unaffected beyond a critical distance. Quantitative analysis shows that odor effectiveness decreases linearly with increased schooling, indicating that collective swimming suppresses, rather than enhances, chemical cue propagation. These insights advance our understanding of biological chemosensory mechanisms and inform the design of bio-inspired robotic systems with enhanced chemical sensing and navigation capabilities.

# Acknowledgements

I would like to express my deepest gratitude to my supervisor, **Dr. Muhammad Saif Ullah Khalid**, for his invaluable guidance, unwavering support, and insightful mentorship throughout my research journey. His expertise, patience, and encouragement have been instrumental in shaping this work and fostering my growth as a researcher. I feel truly fortunate to have had the opportunity to work under his supervision.

I am also sincerely grateful to my thesis committee members, **Dr. Leila Pakzad** and **Dr. Ali Tarokh**, for their time, constructive feedback, and valuable insights, which have significantly contributed to the refinement and improvement of this research. Furthermore, I extend my thanks to **Dr. Chengyu Li** from Case Western Reserve University (CWRU) for his collaboration and support during my research. His contributions and perspectives have enriched the scope and impact of this work.

I wish to pay my heartfelt respects to my parents, **Mr. Muhammad Kamran Chughtai** and **Dr. Zarqa Raiz**, my sister, **Mrs. Maryam Usama**, my brother, **Mr. Muhammad Shanawar**, and most importantly, the person who motivated me the most and stood by me through everything—**my fiancé, Mr. Maaz Ahmad Qureshi**. Without their love, support, and prayers, this work would not have been possible.

I also extend my sincere appreciation to my dear friends **Anum**, **Dania**, and **Iqra**, who supported me through the most challenging phase of my life. Additionally, I would like to acknowledge three incredible women I met in Canada, whose care and compassion made a lasting impact on me: **Mrs. Sabih Raza**, **Mrs. Pakeeza Batool** and **Mrs. Tayyaba Saad**. Their kindness and warmth will always be remembered.

I am grateful to my colleagues and peers who made my transition as an international master's student smooth and welcoming: **Faisal Muhammad**, **Amirhossein Fardi**, **Maryum Waseem**, **Hao Wang**, **Dev Nayak**, and **Dilip Thakur**.

I sincerely acknowledge the financial and computational support provided by **NSERC**, the **Digital Research Alliance of Canada**, **Mitacs**, and **Lakehead University**. Their funding and resources were crucial in the successful completion of this research. I am especially thankful to the **Mitacs Globalink Research Award** for the opportunity to conduct an international research fellowship at **CWRU in Cleveland, Ohio**.

Lastly, I bow in humility before the **Almighty** and thank Him for His countless blessings that have guided and sustained me throughout this journey.

To my beloved parents,

Who have given me the strength, love, and motivation to be where I am today. As someone far from home, I am here because of your prayers, sacrifices, and unwavering belief in me. Your support has been my greatest source of inspiration, and I dedicate this achievement to you both. Your sacrifices have shaped my path, and your love has been my foundation. I am forever indebted to you for everything you have done and continue to do for me.

# Contents

*Chapter 1: Introduction* ..... *1*

**Research Objectives:** ..... **7**

*Chapter 2: Numerical Methodology* ..... *8*

**A. Kinematic Modes** ..... **10**

**B. Flow domain and Geometry** ..... **11**

1. 2D Flow Domain and Geometry: Solitary Swimmer ..... 11
2. 3D Flow Domain and Geometry: Solitary Swimmer ..... 13
3. 3D Flow Domain and Geometry: Fish Schooling ..... 15

**C. Verification** ..... **17**

i) Two-dimensional Verification: ..... 17

ii) Three-dimensional Verification: ..... 20

**D. Validation** ..... **22**

*Chapter 3: Two-Dimensional Vortex-Odor Interaction for Solitary Fish* ..... *25*

- Flow Configuration and Governing Parameters ..... 25
- Analysis of Wake and Vortex Evolution ..... 26
- Odor Transport Dynamics ..... 32
- Role of Convection and Diffusion in Odor Transport ..... 38

*Chapter 4: Three-Dimensional Vortex-Odor Interaction for Solitary Fish* ..... *44*

- Flow Configuration and Governing Parameters ..... 44

- Coupled Vortex–Odor Dynamics ..... 45
- Role of Convection and Diffusion in Odor Transport ..... 51

***Chapter 5: Three-Dimensional Vortex-Odor Interaction for Fish Schooling ..... 54***

- Flow Configuration and Governing Parameters ..... 54
- Coupled Vortex–Odor Dynamics ..... 55

***Conclusions ..... i***

***Future Recommendations ..... iii***

***Bibliography ..... iii***

# List of Figures

Figure 1 Flow domain and the boundary conditions for 2D .....11

Figure 2 Flow domain and non-uniform Cartesian grid for 2D .....12

Figure 3 Physiological model of (a) Jackfish, (b) Eel, and (c) Virtual tunnel, non-uniform Cartesian grid, and the boundary conditions for simulating flows.....14

Figure 4 Geometry of eel and jackfish in the first and second rows, respectively, with four different configurations of fish.....15

Figure 5 Computational domain and mesh with boundary conditions, including an expanded image of Quad-Fish (jackfish) .....16

Figure 6 Results for convergence of (a) grid size and (b) time-step size for 2D .....18

Figure 7 Results for convergence of (a) grid size and (b) time-step size for 3D .....20

Figure 8 Comparison of our results with those of Yan et al. [51] from the transport equation...23

Figure 9 Comparison of our results with those of Khalid et al. [45] .....24

Figure 10 Phase maps illustrating average drag and thrust for both undulating swimmers, (a) and (b) correspond to anguilliform and carangiform swimmers, respectively, at Re = 500, 1000, and 5000.....27

Figure 11 Average drag coefficient values with different $f^*$ at Re = 500, 1000 and 5000 where (a) and (b) correspond to anguilliform and carangiform swimmers, respectively .....28

Figure 12 Vortex configuration at Re = 500, 1000 and 5000 where (a) and (b) correspond to anguilliform and carangiform swimmers, respectively. .....30

Figure 13 Vortex configuration patterns at different time instants during the undulation cycle. The first row corresponds to $t\tau$ = 0, the second row to $t\tau$ = 0.50, and the third row to $t\tau$ = 1.00. Panels (a), (c), and (e) show vortex patterns for anguilliform swimmers; panels (b), (d), and (f) for carangiform swimmers. .....31

Figure 14 Vortex and odor concentration for anguilliform swimmers, with the first and second columns corresponding to vorticity contours and odor concentration, respectively. Panels (a), (b) and (c), (d) display scenarios with a Re = 500 and $f*$ = 0.2 and 0.6, respectively. Panels (e), (f) and (g), (h) display scenarios with a Re = 5000 and $f*$ = 0.2 and 0.6, respectively.....33

Figure 15 Vortex and odor concentration for carangiform swimmers, with the first and second columns corresponding to vorticity contours and odor concentration, respectively. Panels (a), (b) and (c), (d) display scenarios with a Re = 500 and $f*$ = 0.2 and 0.6, respectively. Panels (e), (f) and (g), (h) display scenarios with a Re = 5000 and $f*$ = 0.2 and 0.6, respectively.....34

Figure 16 Overlay plots for vorticity and odor concentration are presented for anguilliform and carangiform swimmers in the first and second columns, respectively. Panels (a), (b) and (c), (d) display scenarios with a Re = 1000 and $f*$ = 0.3 and 0.5, respectively. Panels (e), (f) and (g), (h) display scenarios with a Re = 5000 and $f*$ = 0.3 and 0.5, respectively. .....36

Figure 17 Plot for coordinates of the center of vortices and odor spots for undulating swimmers are displayed in the first and second columns for anguilliform and carangiform swimmers, respectively. Panels (a) and (b) correspond to Re = 1000 and $f*$ = 0.3, while panels (c) and (d) correspond to $f*$ = 0.5 .....37

Figure 18 Odor dynamics for anguilliform swimmers, with the first and second columns corresponding to convection and diffusion, respectively. Panels (a), (b) and (c), (d) display

scenarios with a Re = 500 and $f*$= 0.2 and 0.6, respectively. Panels (e), (f) and (g), (h) display scenarios with a Re = 5000 and $f*$= 0.2 and 0.6, respectively. .....39

Figure 19 Odor dynamics for carangiform swimmers, with the first and second columns corresponding to convection and diffusion, respectively. Panels (a), (b) and (c), (d) display scenarios with a Re = 500 and $f*$ = 0.2 and 0.6, respectively. Panels (e), (f) and (g), (h) display scenarios with a Re = 5000 and $f*$ = 0.2 and 0.6, respectively. .....40

Figure 20 Side-by-side comparison of odorant dynamics, focusing on concentration (first column), convection (second column), and diffusion (third column). Panels (a) through (f) and (g) through (l) represent anguilliform and carangiform swimmers, respectively. Panels (a) to (c) and (g) to (i) show water as the medium, while panels (d) to (f) and (j) to (l) depict air as the medium. .....42

Figure 21 Vortex topology visualized using the Q-criterion with a value of 10, at three different Odor concentration levels. The simulations are performed at Re = 3000 and $f* = 0.4$. The first and second columns represent the results for jackfish (carangiform) and eel (anguilliform) swimmers, respectively. .....46

Figure 22 Odor effectiveness in the wake of Jackfish and Eel: (a) actual and (b) opposite kinematics .....47

Figure 23 Odor plumes for jackfish (first column) and eel (second column) with a different magnification of undulation .....49

Figure 24 Odor effectiveness with a different magnification of undulation: (a) Jackfish and (b) Eel .....50

Figure 25 Influence of convection for Jackfish (first column) and Eel (second column) with a different magnification of undulation .....51

Figure 26 Influence of diffusion for Jackfish (first column) and Eel (second column) with a different magnification of undulation .....53

Figure 27 Vortex topology visualized using the Q-criterion with a value of 10, and odor concentration level at 0.5 for different configurations of eel .....55

Figure 28 Vortex topology visualized using the Q-criterion with a value of 10, and odor concentration level at 0.5 for different configurations of jackfish .....56

Figure 29 Odor effectiveness in the wake of (a) an eel and (b) jackfish .....57

# List of Tables

Table 1 Comparison of $SEe$ for grid-convergence and time-step independence tests for 2D.....19

Table 2 Comparison of $SEe$ for grid-convergence and time-step independence tests for 3D.....21

Table 3 Specifications of governing parameters for 2D .....26

Table 4 Specifications of governing parameters for 3D .....45

# Chapter 1: Introduction

Researchers always get fascinated by how nature designs and adopts a variety of different effective strategies for dealing with complex systems, particularly how animals like fish evolved highly efficient mechanisms for propulsion and navigation. The increasing use of robotic technologies in aerial and aquatic environments for various purposes, including environmental monitoring, search and rescue, and underwater exploration, intensifies research efforts to enhance their efficiency by drawing inspiration from natural designs. Fish are exceptional swimmers, and their ability to flex their bodies in specific ways enables them to achieve remarkable propulsion and maneuverability in aquatic environments. Scientific and engineering community aims to develop robots that can move through water efficiently by understanding the biomechanics and hydrodynamics of fish swimming [1], [2]. Previously, research focused extensively on analyzing propulsive mechanisms of fish and a range of maneuvers achievable by manipulating factors, such as frequency and wavelength [3]. Numerical simulations are pivotal in examining and understanding their dynamics, revealing that the wavelength of undulatory kinematics plays a crucial role in determining the hydrodynamic performance of fish [4]. Recent research studies showed that undulating with larger wavelengths [5] significantly enhanced hydrodynamic thrust for a carangiform swimmer, allowing these fish to conserve energy at an optimal wavelength while maintaining high swimming speeds [6]. In another study, Khalid et al. [7] reported that anguilliform swimmers were able to attain better hydrodynamic performance metrics by performing the wavy motion at a smaller wavelength than their body-lengths. These findings demonstrate the diversity and effectiveness of different biological propulsive techniques

in different marine animals. Additionally, researchers investigated the influence of body shape and adaptive kinematics [8] to gain deeper insights into both propulsion and navigation capabilities. Excellent reviews of these research investigations, laying the groundwork for hydrodynamic designs of bio-inspired underwater robots were presented by Fish & Lauder [9], [10], Lauder [11], Fish [12], Zhang et al. [13], and Raj and Thakur [14].

Fish live and propel themselves in challenging marine environments using a sophisticated combination of sensory modalities for underwater sensing, detection, and navigation [15]. Researchers are keen to unravel the mysteries of aquatic locomotion and sensory perception to develop autonomous underwater vehicles (AUVs) that can mimic these natural abilities. Fish employ a diverse approach to gather information about their surroundings, utilizing visual inspection, olfaction detection of chemical cues, acoustic perception, and sensitivity to pressure fluctuations through their lateral line system [16]. Visual inspection allows fish to perceive their environment, detect obstacles, and identify potential preys or predators [17]. Besides, olfaction plays a crucial role in detecting chemical cues emitted by food sources, potential mates, or nearby predators, aiding in migration and foraging behaviors [18]. Acoustic perception enables fish to sense disturbances in the water and communicate with conspecifics, contributing to social interactions and strategies for avoiding predators [19]. Additionally, the sensitivity of fish scales on their bodies to pressure changes facilitates precise control of directionality and locomotion through water, enhancing their ability to perform complex maneuvers [20].

Despite many advancements in understanding fish locomotion during the last two decades, the important role and influence of olfactory cues, integrated with hydrodynamics, in fish swimming remained an entirely unexplored aspect [21], [22]. The interaction between

hydrodynamics and chemosensory systems in fish is an emerging field of study that holds potential for significant discoveries [23]. To the authors' best knowledge, almost no studies were devoted to examining the effects of chemical cues on fish locomotion [24]. Only one recent research study by Menzer et al. [25] addressed this important subject, who concluded that olfactory chemoreception in a fish-like school and the associated hydrodynamic interactions played a crucial role in collective behavior and navigation. While it is well-established through research investigations from biologists [21] that fish utilizes chemical cues for directional control during navigation in water, this phenomenon was predominantly examined for odor dynamics and aerodynamics of flying insects [26], [27], [28]. However, a critical knowledge gap exists regarding the potential connection between fluid dynamics and odor dynamics around undulating bodies. To address this important aspect related to biological propulsion in our present work, we employ computational methods using our in-house solver, developed based on Immersed-Boundary Method (IBM) and named as IBVortX [29]. With the recent advancements in developing olfactory sensing technology [30], its integration with insightful information about fluid dynamics carries significant potential to revolutionize the design of bio-inspired underwater robots [31], enabling them to become more efficient, adaptive, and capable of performing complex tasks in challenging underwater environments. Mimicking the natural strategies of fish and leveraging their sensory capabilities, autonomous robotic systems can be made to respond intelligently to environmental cues [32] in diverse aquatic conditions, contributing to marine biology, environmental conservation, and oceanographic exploration. Therefore, combining vortex dynamics with odor dynamics around undulating bodies fundamentally sets up the novelty and the main objective of our current work.

To further elaborate on the research questions associated with the primary aim of our work, we address the following key aspects: (i) how do odor dynamics couple with vortex dynamics around undulating bodies in water? (ii) how do diffusion and convection of odor compare in a fluid medium for bio-inspired propulsion? (iii) what roles do the physiology and kinematics of biological swimmers play in spreading and suppressing their odors in the wake? (iv) how does fish schooling influence the suppression or dispersion of odor in a vortical wake? To answer these research questions, we first conduct a two-dimensional Vortex-Odor Interaction study, followed by a three-dimensional Vortex-Odor Interaction analysis, and finally, an investigation into the influence of fish schooling. This research is structured into three chapters, corresponding to Chapters 2, 3, and 4.

It is important to highlight that our present work is the first study that involves the computational modeling of both diffusion and convection phenomena in determining the unsteady behavior and transport of a chemical specie at both high and low values of Schmidt numbers [26], [27]. Unlike previous studies[33], [34], which focused solely on unsteady propulsion, our work pushes the boundaries of the field by exploring how unsteady flow impacts chemical distribution in the fluid environment.

There are different classifications of marine species based on their physiology and kinematics [2]. These include anguilliform, carangiform, sub-caragiform, thunniform, and ostraciiform. Our work is focused on two primary modes, including carangiform and anguilliform. For two-dimensional Vortex-Odor Interaction, we consider viscous and transitional flow regimes, defined through Reynolds numbers ($Re$) of 500, 1000, and 5000 [3] along with Strouhal number ($St = \frac{fA_{tail}}{U_\infty}$), where $f$ denotes the excitation or flapping frequency of the caudal fin, and $A_{tail}$ is

the maximum one-sided oscillation amplitude of the caudal fin, ranging from 0.2 to 0.6. Here, we characterize fluid media, water and air, through Schmidt number ($Sc = \frac{\nu}{D}$), which is the ratio between kinematic viscosity $(\nu)$ of a fluid and diffusivity (D), of an odor. Even though fish primarily inhabit aquatic environments, testing the solver's robustness in both water and air is essential for comprehensive validation and verification. For three-dimensional Vortex-Odor Interaction, our simulations focus on transitional flow regimes with a Reynolds number of 3000 and Strouhal numbers ($\mathrm{St} = 0.25\ and\ 0.40$) combined with the Schmidt number to characterize odor transport in water. These investigations offer valuable insights into how swimmer kinematics, flow conditions, and medium properties influence the distribution of chemical cues. Understanding the relationship between vortex dynamics and odor transport has significant implications for underwater sensing and robotics. By mimicking the natural strategies of fish, bio-inspired robotic systems can integrate hydrodynamic and chemical sensing capabilities to perform complex tasks in challenging aquatic environments. This work advances the state of the art by addressing the role of both 2D and 3D vortex dynamics in odor dispersal and offering a comprehensive framework for multi-physics simulations. Our findings are expected to contribute to the fields of marine biology, environmental conservation, and oceanographic exploration, while also aiding in the development of efficient and adaptive underwater robotic systems [31], [32].

To elaborate our approach of performing two-dimensional (2D) simulations before moving onto 3D simulations in this work, we emphasize that recent advances in experimental [35], [36] and computational methods [37], [38] enabled scientists to capture and analyze complex three-dimensional (3D) flow features around these remarkable biological species,

helping to identify how these flows generate the fluidic forces essential for their propulsion and maneuverability. Despite these developments, the high cost of these techniques attached with computational requirements and time still restricts our ability to conduct extensive parametric studies across a broad range of parameters. In this context, 2D simulations provide valuable insights into the fundamental characteristics of fluid flows around undulating swimmers. To interpret the results of 2D simulations, one can consider the extraction of flow fields along the mid-planes of virtual swimmers with infinitely wide bodies. Past research work [39], [40], [41] also investigated the conditions under which conclusions from 2D simulations could apply to 3D flows. For instance, Liu et al. [39] conducted both 2D and 3D simulations for flows around a tadpole, finding minimal vertical crossflow along the dorsal and ventral tail fins, with flow characteristics along most of the body and tail remaining largely 2D. Similarly, Gazzola et al. [42] identified optimized kinematic patterns for the C-start motion of a zebrafish larva that aligned with experimentally observed movements [43], based on both 2D and 3D analyses. More recently, Zurman-Nasution et al. [41] used an oscillating NACA0016-shaped wing at Re = 5300 to determine the range of Strouhal numbers where 3D vortex features become significant, concluding that flow over pitching wings remained mainly 2D for Strouhal numbers up to 0.60. These findings directly justify our computational approach for this study.

## *Research Objectives:*

The following are the primary objectives of this research:

- To investigate how vortex dynamics influence odor transport in underwater sensing scenarios.
- To analyze how the nature of the fluid medium (e.g., water vs. air) affects the diffusion and convection mechanisms governing odor dispersion.
- To determine whether fish schooling behavior amplifies or suppresses the effectiveness of odor signals.

# Chapter 2: Numerical Methodology

The mathematical model for fluid flow is based on the following non-dimensional forms of the continuity and incompressible Navier-Stokes equations[29], [48].

$$\frac{\partial u_j}{\partial x_j} = 0 \ (1)$$

$$\frac{\partial u_i}{\partial t} + u_j \frac{\partial u_i}{\partial x_j} = -\frac{1}{\rho}\frac{\partial p}{\partial x_i} + \frac{1}{Re}\frac{\partial^2 u_i}{\partial x_j \partial x_j} + f_b (2)$$

where $i, j = 1,2,3$, $x_i$ shows Cartesian directions, $u_i$ denotes the Cartesian components of the fluid velocity, $p$ is pressure, and Re represents Reynolds number. For the current numerical formulation, the term $f_b$ shows a discrete forcing term, allowing for a sharp representation of the immersed boundary [48].

We solve the governing mathematical model for fluid flows using a sharp-interface immersed boundary method on a non-uniform Cartesian grid, with radial-basis functions as the interpolation scheme to precisely identify the immersed bodies [29]. We use a central difference scheme for spatial discretization to approximate the diffusion term, while the convection term is discretized using the Quadratic Upstream Interpolation for Convective Kinematics (QUICK) scheme. The integration with respect to time is carried out through a fractional-step method, ensuring second-order accuracy in both time and space. The prescribed wavy kinematics are applied as a boundary condition on the swimmer's body, enforced on immersed bodies through a ghost-cell technique[29], [48] suitable for both rigid and flexible structures. Further details on this fully parallelized solver and its application to various bio-inspired fluid flow problems can be

found in the work of Farooq et al [29]. Neumann boundary conditions are applied at the far-field boundaries, except for the left-sided inlet boundary of the domain, where Dirichlet conditions are used for the in-flow.

Odor concentration refers to the chemical cues released in a fluid medium, which can indicate the presence of prey, predators, or potential mates, thus aiding in chemical sensing for navigation, foraging, and communication. These chemical signals consist of various molecules, such as amino acids, pheromones, and metabolic waste products, which diffuse through aerial and aquatic environments. After computing the velocity field $u_i$, the odor transport equation is solved to determine the instantaneous odor concentration field in the whole computational domain. The governing unsteady equation for the convection and diffusion of the odorant is provided below:

$$\frac{\partial C}{\partial t} + u_i \frac{\partial C}{\partial x_i} = D \frac{\partial^2 C}{\partial x_i \partial x_i} \quad (3)$$

where $C$ is the odor concentration, nondimensionalized by the source odor concentration at the body surface of swimmers, and $D$ is the diffusivity of odor. To numerically approximate the temporal (first term on the left side), convective (second term of the left side), and diffusion terms (the only term on the right side) in Equation. 3 using the same computational schemes for temporal and diffusion terms that we employ to compute the analogous terms in the Navier-Stokes Equation 2. We solve the convective term using the upwind scheme. We explain the role of convection and diffusion processes in transport of odor in the flow field using the respective terms in Equation 3. Our robust approach enables us to perform multi-physics computational simulations, involving fluid-structure-chemical interactions, with very high values of Schmidt number accurately and efficiently.

## A. Kinematic Modes

For our extensive research, we consider two types of wavy kinematic modes: anguilliform and carangiform. Anguilliform swimmers, such as eels, move by undulating a large portion of their bodies, while carangiform swimmers, like certain fish species, have prominent caudal fins attached to their bodies [44]. The amplitude of the carangiform profile, where the chord represents a fish's backbone, is described by the following relation [3], [5], [45]:

$$A\left(\frac{x}{L}\right) = 0.02 - 0.0825\left(\frac{x}{L}\right) + 0.1625\left(\frac{x}{L}\right)^2 ; 0 < \frac{x}{L} < 1 (4)$$

where $x$ denotes the stream-wise coordinate of each node used to discretize the model swimmer, and $A(x/L)$ shows the local amplitude at a given spatial position along the swimmer's body, nondimensionalized by its total length $(L)$. This body length is equal to the chord of the foil for our 2D, and 3D simulations. Here, the coefficients are calculated based on the data provided for a steadily swimming saithe fish, which is a carangiform swimmer [46] with local amplitudes of $A(0) = 0.02, A(0.2) = 0.01, and\ A(1.0) = 0.10$. Limiting the maximum amplitude of the trailing-edge to $0.10$ for the two swimmers, we define the amplitude envelop of anguilliform kinematics using the following relation [3], [7], [47]:

$$A\left(\frac{x}{L}\right) = 0.0367 + 0.0323\left(\frac{x}{L}\right) + 0.0310\left(\frac{x}{L}\right)^2 ; \quad 0 < x/L < 1 (5)$$

Using $f$ being the oscillation frequency and $t$ as the time, the undulatory motion in both the cases is modeled by the following mathematical form:

$$y\left(\frac{x}{L}\right) = A\left(\frac{x}{L}\right) sin\left[2\pi\left(\frac{x}{\lambda} - ft\right)\right] (6)$$

## B. Flow domain and Geometry

To support the evolving scope of this research, we defined different flow domains and geometric configurations tailored to each phase of the investigation. These configurations were designed to match the increasing complexity of our study—from two-dimensional analysis of solitary swimmers to fully three-dimensional simulations involving multiple swimmers in schooling formations. Each setup captures the essential fluid-structure and chemical interaction mechanisms required to investigate the research objectives.

### 1. 2D Flow Domain and Geometry: Solitary Swimmer

For 2D simulations, we use the NACA0012 foil to model the bodies of swimmers, with the chord representing a swimmer's spine during static equilibrium. The swimmer is positioned in a rectangular virtual tunnel, as illustrated in Figure 1, with dimensions of the flow domain set to as $34L \times 18L$. Please note that the Figure 1 is not intended to be according to a scale but rather to highlight the geometric details.

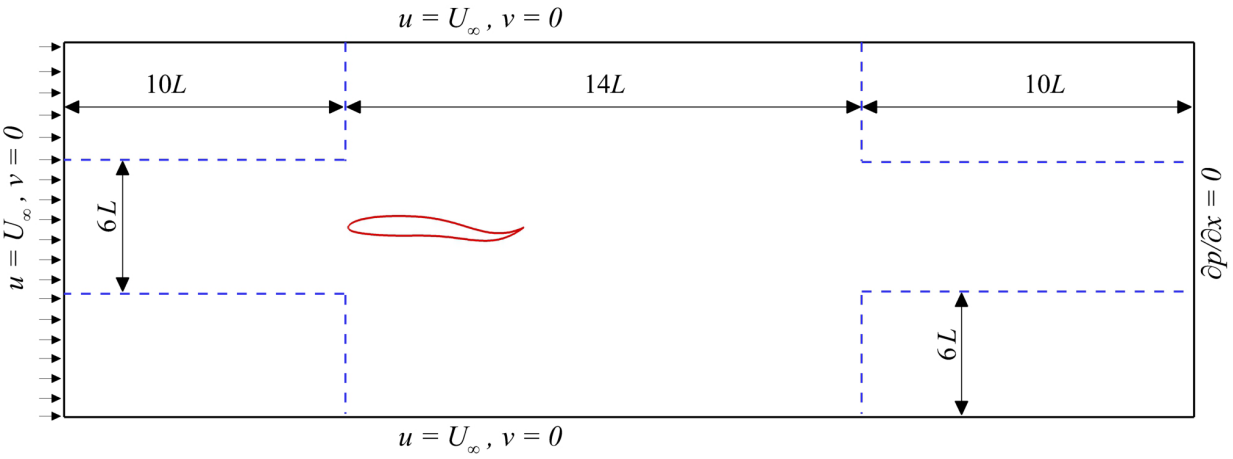


*Figure 1 Flow domain and the boundary conditions for 2D*

We design the mesh with two distinct regions, as depicted in Figure 2, a finer region and a coarser region. The finer region is generated uniformly based on the number of elements specified for this region. To ensure a smooth transition between the fine and coarse regions, we first define the variable (ϕ), which is linearly spaced between 0 and 1, according to the number of elements in the coarse region. To achieve non-uniformity and smooth gradation, we modify this meshing parameter using the following formulation:

$$\phi = (1 - \phi) \cdot (1 + \phi)(1)$$

This transformation creates a non-uniform distribution of points. The spacing between elements is then adjusted with the following equation to provide a smooth transition:

$$x_\phi = \left(d_{xc} - d_{xf}\right) \cdot \phi + d_{xf}(2)$$

where $(d_{xc})$ is the spacing between elements in the coarse region, and $(d_{xf})$ is the spacing between elements in the finer region. This formulation ensures a smooth and gradual change from fine to coarse grid cells.

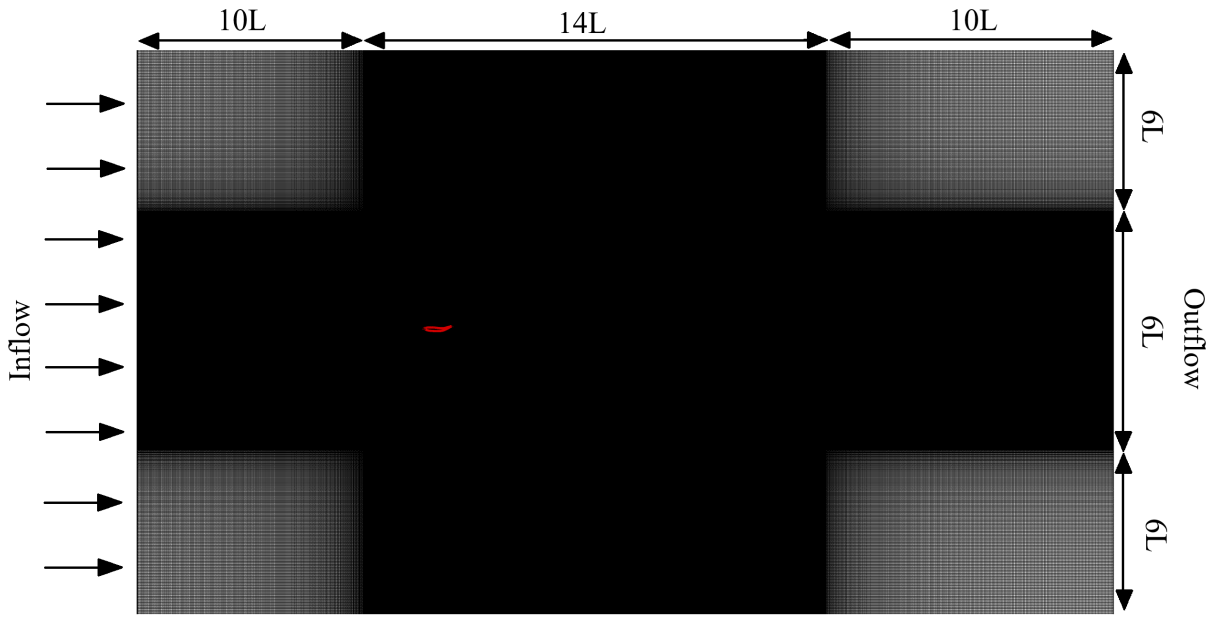


*Figure 2 Flow domain and non-uniform Cartesian grid for 2D*

## *2. 3D Flow Domain and Geometry: Solitary Swimmer*

Moving our research from 2D to 3D simulations, we use the real geometries of a Jackfish and an eel, as shown in Figure 3a-Figure 3b, to represent two wavy kinematic modes: carangiform and anguilliform, respectively. Carangiform swimmers, such as Jackfish, possess prominent caudal fins attached to their bodies [44], while anguilliform swimmers, like eels, undulate a large portion of their slender bodies to generate movement. In this work, the total height and width of the Jackfish are 0.3021L and 0.1481L, respectively, where L is the total length of the fish. The area of its body is $0.4479L^2$. It is important to note that median fins, such as the dorsal and anal fins, are not considered in this study, as their total effect is less than $5\%$ of the forces, as discussed by Liu et al. [53]. The total height and width of the eel are 0.0884L and 0.0605L, respectively whereas the body has a surface area of $0.1739L^2$. The geometry of the Jackfish is comprised of the trunk and caudal fin[5], where the trunk is discretized using 22,712 triangular elements and 11,358 nodes, while the caudal fin alone consists of 2,560 triangular elements and 1,369 nodes. The eel's geometry is represented using 33,112 triangular elements and 16,558 nodes[7].

Each swimmer is positioned in a virtual tunnel to simulate flows over it, with the flow domain dimensions illustrated in Figure 3c. The dimensions of the flow domain are set to $10L \times 4L \times 4L$, where L represents the total length of the swimmer. We use the same approach as aforementioned (Chapter 3: Two-Dimensional Vortex-Odor Interaction) [49] to design the non-uniform mesh with two distinct regions, as shown in Figure 3c: a finer region and a coarser region.

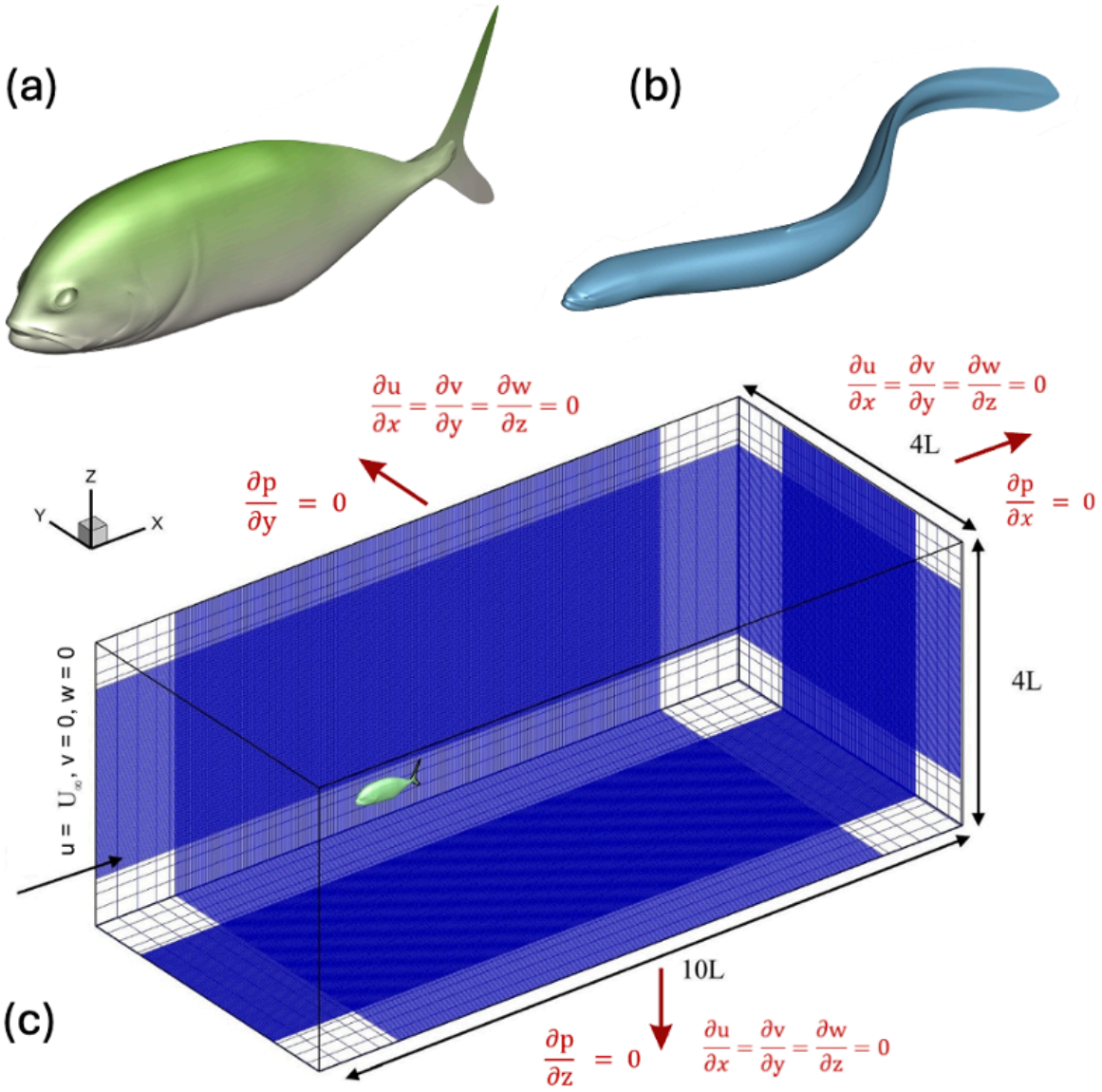


*Figure 3 Physiological model of (a) Jackfish, (b) Eel, and (c) Virtual tunnel, non-uniform Cartesian grid, and the boundary conditions for simulating flows*

### 3. *3D Flow Domain and Geometry: Fish Schooling*

For fish schooling, we use four different configurations of fish, as shown in Figure 4. These configurations include an individual fish, known as Mono-Fish (Figure 4a), and a group of fish, referred to as Bi-Fish (Figure 4b), Tri-Fish (Figure 4c), and Quad-Fish (Figure 4d). We use the real geometries of an eel and a jackfish to represent two wavy kinematic modes: anguilliform and carangiform, respectively[49].

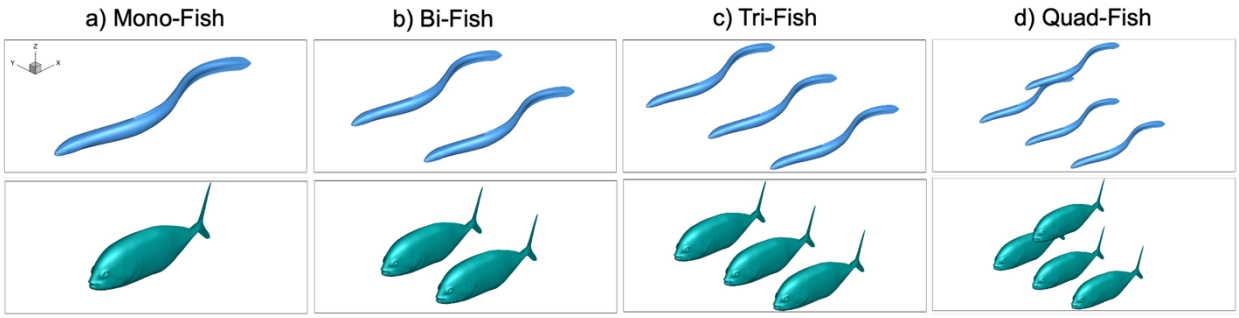


*Figure 4 Geometry of eel and jackfish in the first and second rows, respectively, with four different configurations of fish*

Each swimmer is positioned in a virtual tunnel to simulate flows over it, with the flow domain dimensions illustrated in Figure 5. The dimensions of the flow domain are set to $10L \times 4L \times 4L$, where L represents the total length of the swimmer. We use the same approach as Kamran et al. [49] to design the non-uniform mesh with two distinct regions, as shown in Figure 5: a finer region and a coarser region. In this work, we use a grid with 30 million nodes and perform simulations using 2000-time steps per undulation cycle.

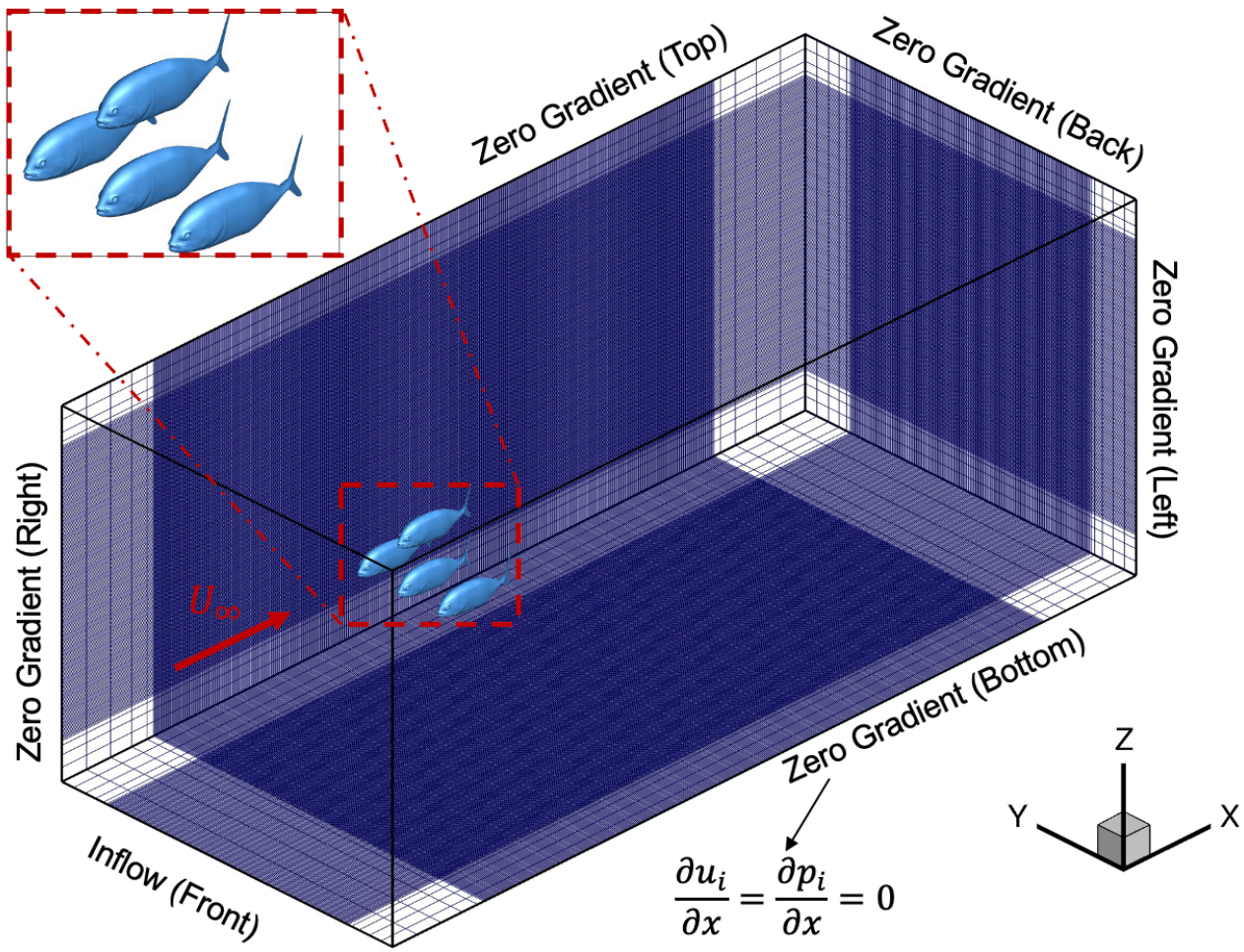


*Figure 5 Computational domain and mesh with boundary conditions, including an expanded image of Quad-Fish (jackfish)*

## C. Verification

### i) Two-dimensional Verification:

Before performing our multi-physics simulations for the current work, we carry out an extensive set of grid-independence and time-step convergences studies. For this purpose, we employ a NACA-0012 foil by prescribing a carangiform waveform over its surface [3], characterized by an undulation wavelength ($\lambda$) of 1.05. Please note $\lambda$ that is nondimensionalized by the chord-length of the foil, and the Reynolds number defined by Re $= U_\infty L/\upsilon$ is set as $10^3$. Here, $U_\infty$ and L denote the free-stream velocity of the flow and chord-length of the foil, respectively. We conduct these simulations for a Strouhal number ($St = \frac{fA_{tail}}{U_\infty}$) St = 0.40. First, we complete the grid-independence test using three different grid configurations using a time-step ($\Delta t$) according to 2000 time-steps per oscillation cycle. Grid 1, grid 2, and grid 3 have sizes of 1597×1135, 1747×1201, and 1975×1273, respectively.

Figure 6a exhibits comparisons between the instantaneous lift and drag coefficients, represented by $C_L$and $C_D$ of the undulating foil for its one undulation cycle, where τ is the time-period of the undulation. Here, the profiles of the force coefficients qualitatively look very similar for the three grids during the $15^{th}$ cycle, where the solutions become steady state within 5-6 oscillation cycles. In this study, we focus on global aerodynamic characteristics—specifically drag and lift coefficients—as indicators for grid convergence. Although velocity profiles can be used to study localized flow behavior, they are often limited to pointwise or region-specific analysis and may not represent the full domain behavior. Since our objective is to validate grid independence for the entire computational domain and the resultant force effects on the body,

we rely on the evolution of $C_L$and $C_D$, which effectively capture the integrated influence of the flow field.

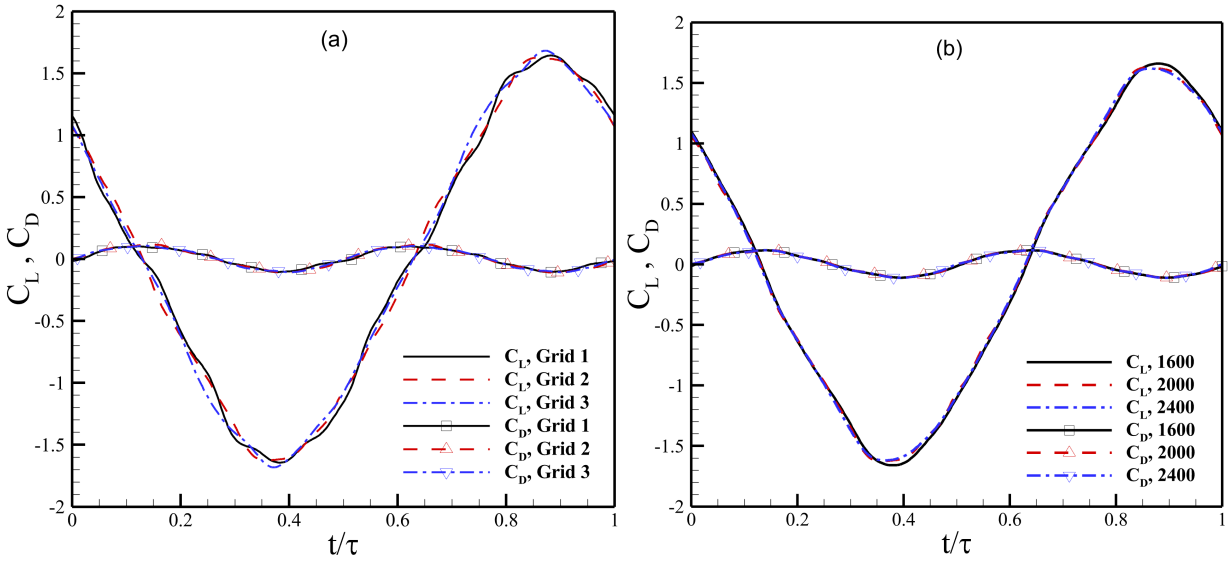


*Figure 6 Results for convergence of (a) grid size and (b) time-step size for 2D*

In order to make an adequate choice of the grid for our next simulations and to better evaluate the convergence of our results, we quantify the difference between the three solutions through a parameter called the standard error of estimate $(SE_e)$. It is mathematically defined as:

$$SE_e = \sqrt{\frac{\sum\left(Y_{\text{obs}} - Y_{\text{pred}}\right)^2}{n-p}} \quad (9)$$

where $(Y_{\text{obs}})$ represents the observed values, $(Y_{\text{pred}})$ shows the predicted values, n is the number of observations, and p is the number of parameters. Choosing the results obtained from Grid 3 as the reference ones $\left(Y_{\text{pred}}\right)$, Table 1 clearly reflects smaller differences between the results obtained from Grid 2 and Grid 3 for both $C_L$ and $C_D$. Therefore, we proceed with Grid 2 for our next set of simulations. For the time-step independence study, we choose three values of

$\Delta t, \Delta t_1, \Delta t_2, and\ \Delta t_3$, according to 1600, 2000, and 2400 time-steps, respectively, in each oscillation cycle. The results in terms of $C_L$and $C_D$ are presented in Figure 6b, where we find the three profiles of each force coefficient to be very similar. In order to further ensure the convergence of $\Delta t$ using the smallest $\Delta t$ as the reference values (Time-step 3 in this case), values of $SE_e$ are shown in Table 1. It is clear that the difference in results between the simulations for $\Delta t_2\ and\ \Delta t_3$ is reduced compared to those from $\Delta t_1 and\ \Delta t_3$. Hence, the remaining simulations for this work are performed using 2,000 time-steps per undulation cycle.

*Table 1 Comparison of $SE_e$ for grid-convergence and time-step independence tests for 2D*

| | Grid-independence Tests | | Time-step Convergence Tests | |
|---|---|---|---|---|
| | Grid 1 & Grid 3 | Grid 2 & Grid 3 | $\Delta t_1$ & $\Delta t_3$ | $\Delta t_2$ & $\Delta t_3$ |
| Drag coefficient ($C_D$) | 0.8221 | 0.5838 | 0.4393 | 0.2475 |
| Lift coefficient ($C_L$) | 6.0575 | 5.8059 | 2.5258 | 1.1156 |

### *ii) Three-dimensional Verification:*

For three-dimensional analysis similar approach was used. We perform extensive grid-independence and time-step convergence studies. For this purpose, we use the geometry of a Jackfish with prescribed carangiform kinematics [3] characterized by an undulation wavelength (λ) of 1.05. Reynolds number is set to 3000, and Strouhal number (St $or$ $f*$) is 0.40. The grid-independence test is conducted using three grid configurations and a time-step ($\Delta t$) corresponding to 2000 time-steps per oscillation cycle. The grid sizes are defined as $505 \times 209 \times 209$ $(Grid\ 1), 553 \times 217 \times 217$ $(Grid\ 2), and\ 601 \times 225 \times 225$ $(Grid\ 3)$, corresponding to approximately 20 million, 25 million, and 30 million mesh nodes, respectively.

Figure 7a shows the comparison of instantaneous lift and drag coefficients ($C_L$ and $C_D$) for one complete undulation cycle, where $\tau$ is the time-period of the undulation. The force coefficient profiles for the three grids are qualitatively similar during the $15^{th}$ cycle, after steady-state conditions are achieved within 5–6 oscillation cycles.

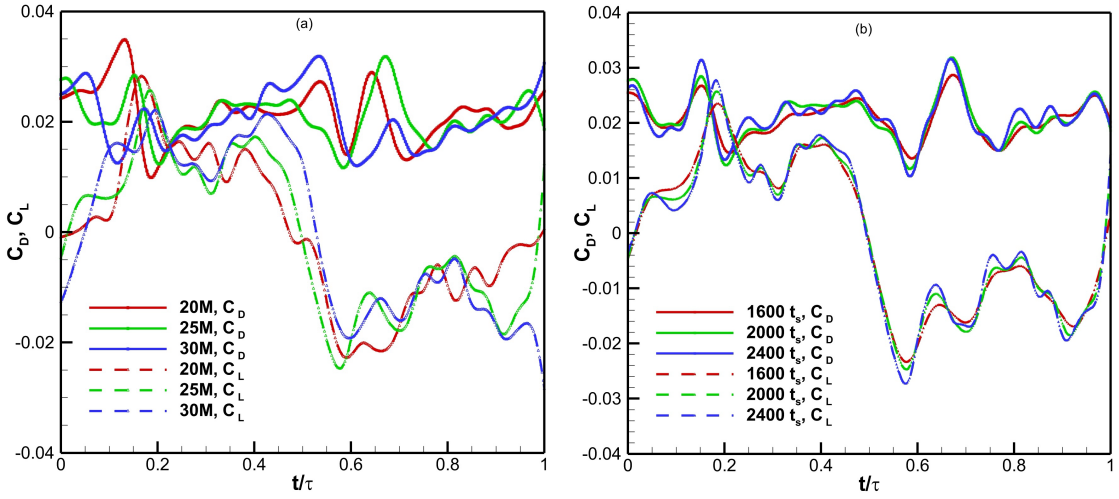


*Figure 7 Results for convergence of (a) grid size and (b) time-step size for 3D*

To evaluate grid convergence and select an appropriate grid for further simulations, we calculate the standard error of estimate ($SE_e$), defined as aforementioned[49]. Using the results from Grid 3 as reference $\left(Y_{\text{pred}}\right)$, shows smaller differences between the results obtained from Grid 2 and Grid 3 for both $C_L$and $C_D$. Consequently, we select Grid 2 with 25 million nodes for subsequent simulations.

For the time-step convergence study, we test three time-step sizes, $\Delta t_1, \Delta t_2, and \Delta t_3$, corresponding to 1600, 2000, and 2400 time-steps per oscillation cycle. The results of $C_L and C_D$ are shown in Figure 7b for three simulations. The force coefficient profiles are very similar for all three time-steps. Using the smallest time-step size ($\Delta t_3$) as the reference, Table 2 illustrates that the differences in results are smaller between $\Delta t_2$ and $\Delta t_3$ than that between $\Delta t_1$ and $\Delta t_3$. Therefore, the remaining simulations in this work are performed using 2000 time-steps per undulation cycle.

*Table 2 Comparison of $SE_e$ for grid-convergence and time-step independence tests for 3D*

| | Grid-independence Tests | | Time-step Convergence Tests | |
|---|---|---|---|---|
| | Grid 1 & Grid 3 | Grid 2 & Grid 3 | $\Delta t_1$ & $\Delta t_3$ | $\Delta t_2$ & $\Delta t_3$ |
| Drag coefficient ($C_D$) | 1.0453 | 0.88467 | 0.37801 | 0.25764 |
| Lift coefficient ($C_L$) | 1.5462 | 1.1158 | 0.63192 | 0.4343 |

## *D. Validation*

To validate the accurate functionality of the transport equation (Equation 3), we adopt the route suggested by Lei et al. [50]. The structure of the advection-diffusion equation for transport of an odor is the same as that of the energy equation. In Figure 8, we present the comparison of our results in terms of odor concentration ($C^*$, nondimensionalized by the strength of odor of the source that is the foil in this study) for a 2D flow around a rotating cylinder with the results obtained by Yan et al. [51], who used their computational tool developed based on Lattice-Boltzmann method. These results are obtained for Re = 200 and a reduced frequency of 0.5. A good match between the two instantaneous profiles of the dependent parameters versus $X^*$ (the x-coordinate nondimensionalized by radius of the cylinder) demonstrates the effectiveness of our solver. To support this qualitative agreement with quantitative evidence, we compute the Root Mean Square Error (RMSE) between our results and those from Yan et al. [51], obtaining a value of 0.1948. This level of error is reasonable given the methodological differences between the two approaches: our solver is based on the immersed boundary method (IBM), while the reference study employed the Lattice-Boltzmann method (LBM). Despite these differences in numerical formulation, the comparison confirms the validity and accuracy of our solver. Furthermore, our IBM-based computational framework has undergone extensive validation in recent work by Farooq et al. [29], further supporting its reliability in solving similar transport problems.

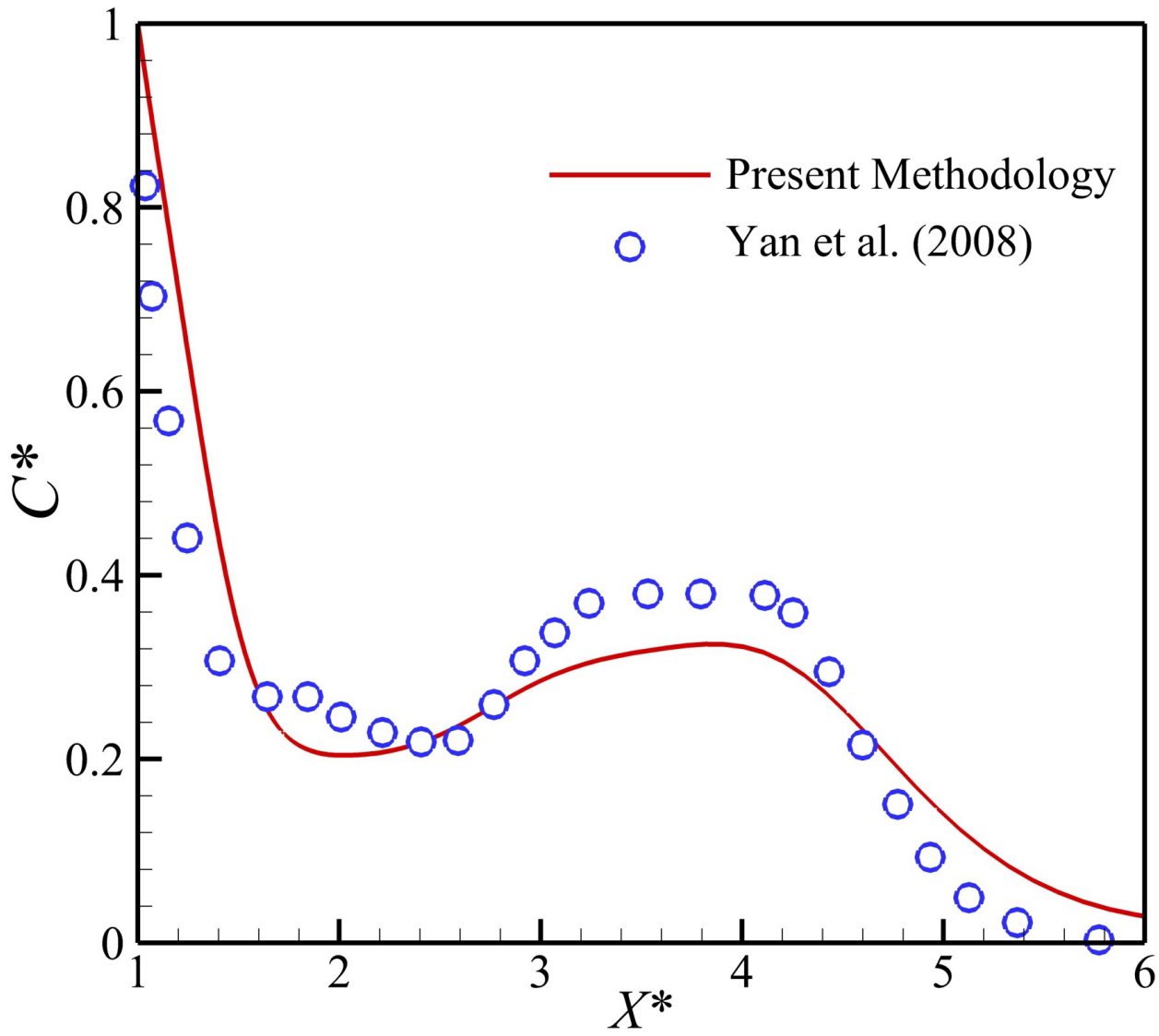


*Figure 8 Comparison of our results with those of Yan et al. [51] from the transport equation*

In addition, we validated our three-dimensional simulation results against the data reported by Khalid et al.[45], who used a non-membranous undulatory swimmer body in their simulations. As shown in Figure 9, we compare the time evolution of drag coefficients ($C_D$) for two elongation ratios, $\lambda = 0.95$ and $\lambda = 1.1$, at Re = 3000 and $f^*$ = 0.4. The oscillatory trends in our results closely match those of Khalid et al [45]. Minor discrepancies can be attributed to the

difference in body geometry—our swimmer model is membranous with zero thickness, while the reference study used a non-membranous body, which affects the wake structure.

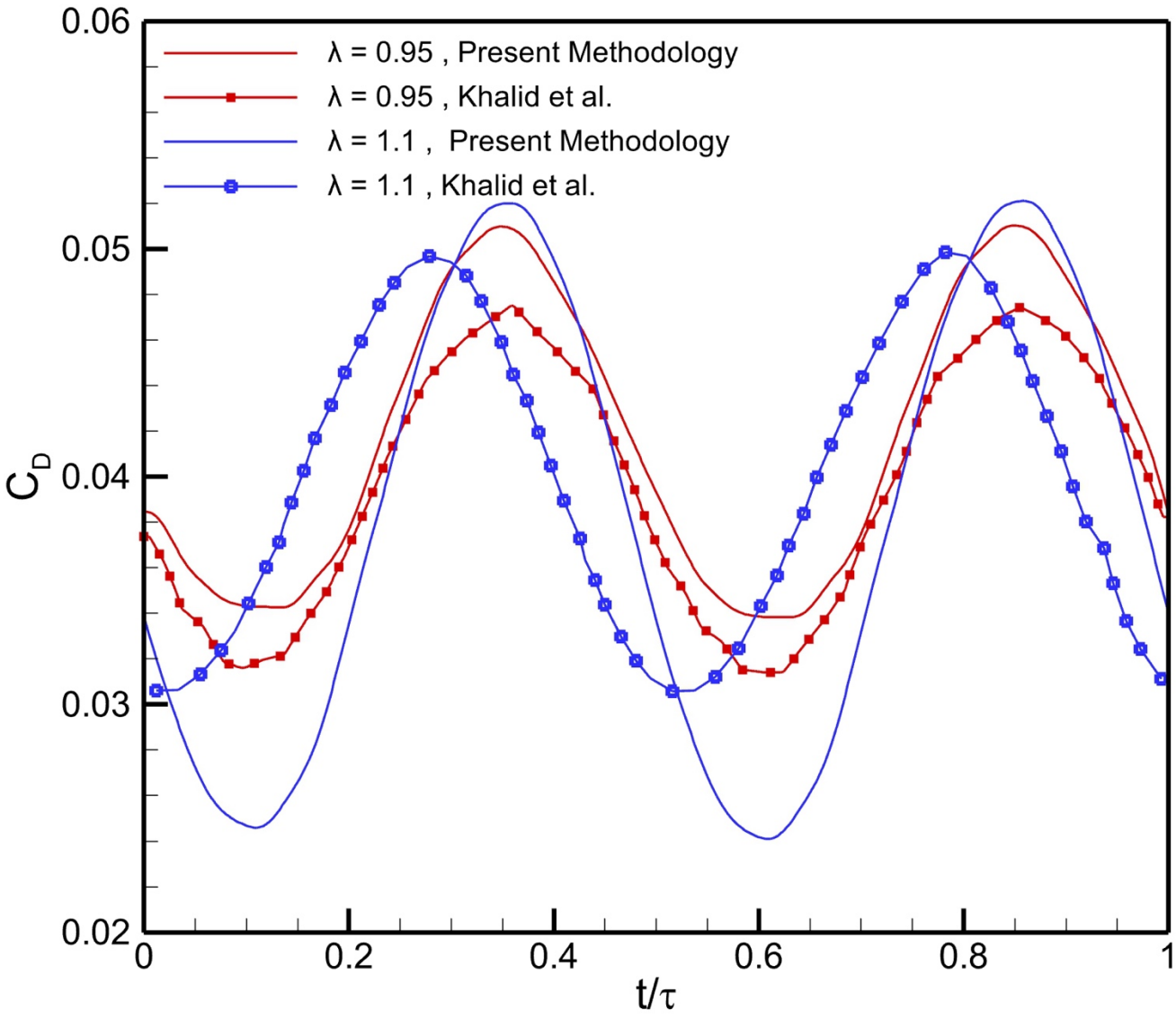


*Figure 9 Comparison of our results with those of Khalid et al. [45]*

# Chapter 3: Two-Dimensional Vortex-Odor Interaction for Solitary Fish

This chapter investigates the coupling between vortex dynamics and odor transport around undulating bodies in two-dimensional fluid environments, using an in-house Immersed Boundary Method (IBM) solver. Simulations are performed for carangiform and anguilliform swimmers in both water and air, highlighting the influence of waveform and medium properties on chemical cue dispersion. Results reveal that odor transport is largely governed by convective mechanisms in water and by a combination of convection and diffusion in air. Odor fields show partial overlap with vortex structures, but the alignment is not exact, indicating a complex transport relationship. The findings contribute to the foundational understanding of chemosensory-driven propulsion and serve as a baseline for more advanced three-dimensional studies.

- *Flow Configuration and Governing Parameters*

To find answers to specific research questions, defined in 'Chapter 1: Introduction', related to coupled vortex dynamics and transport of chemical cues, we perform simulations for flows and odor dynamics around 2D undulating bodies. The details of the governing flow, kinematic, and odor-related parameters are provided in Table 3. We run these simulations using three different values of Re, indicating viscous and transitional flow regimes [3]. Two different waveforms, anguilliform and carangiform, are prescribed to define undulation of the body [3] at

$f^*$, ranging from 0.2 to 0.6 with a gap of 0.05, as marine animals mostly swim in this range [3].We define two different fluid media using Sc as 340 (for water) and 0.7 (for air). These specifications make the total number of simulations as 108 for our present work. It is important to mention that we employ λ = 0.75 for the anguilliform kinematic mode [7] and λ = 1.05 for the carangiform one[5].

*Table 3 Specifications of governing parameters for 2D*

| Parameters | Specifications |
|---|---|
| Geometry | NACA-0012 |
| Undulatory kinematics | Anguilliform and Carangiform |
| Re | 500, 1000, and 5000 |
| Sc | Water (340) and Air (0.7) |
| $f^*$ | 0.2 - 0.6 |
| $\lambda$ | 0.75 and 1.05 |

- *Analysis of Wake and Vortex Evolution*

We begin the discussion on our results using qualitative and quantitative analyses of hydrodynamic performance metrics for both anguilliform and carangiform swimmers. In the form of phase maps, Figure 10 provides distinct combinations of Re and $f^*$ that produce overall drag and thrust forces. The information corroborates with the findings of Khalid et al. [3] in terms of showing the production of thrust at $f^* \geq 0.5$. This critical value of Strouhal number decreases, as we increase Re, slowly for anguilliform swimmer and more aggressively for the carangiform one. We calculate transient and time-averaged $(C_D) and (C_L)$ by dividing the corresponding hydrodynamic forces by dynamic pressure $(0.5\rho U_\infty^2 L)$. We compute the hydrodynamic forces by

integrating pressure and shear stress over the surface of the undulating foil. Using the time-period of an undulation cycle $\left(\tau = \frac{1}{f}\right)$, we utilize the following equation:

$$\overline{C} = \frac{1}{\tau}\int_{t}^{t+\tau} C(t)\ dt (10)$$

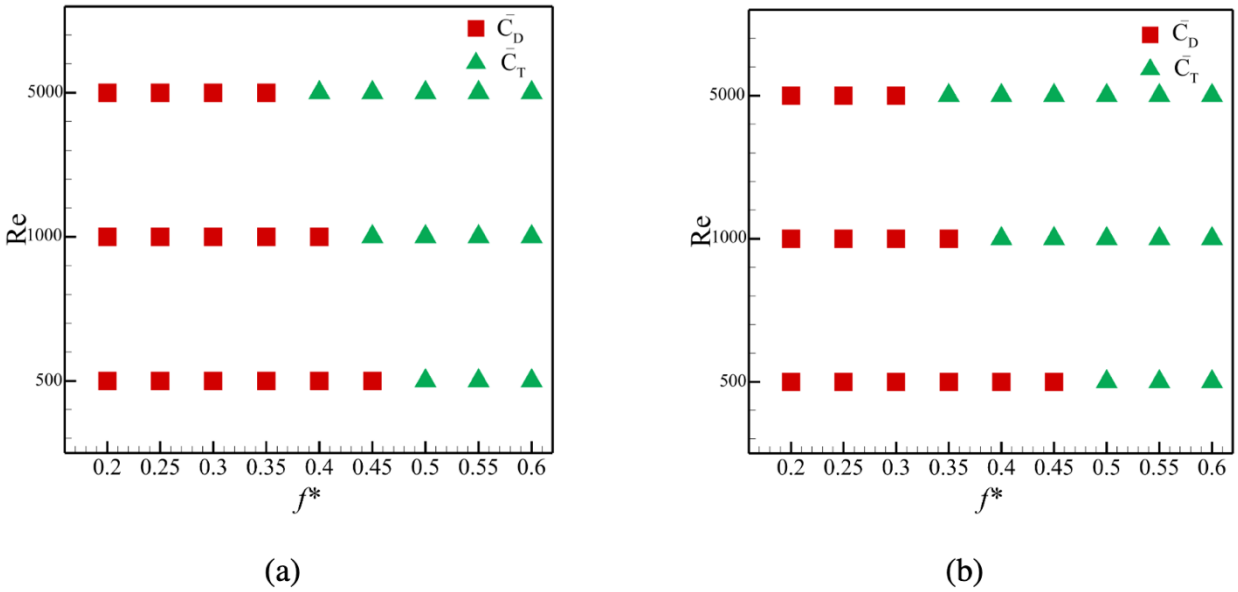


*Figure 10 Phase maps illustrating average drag and thrust for both undulating swimmers, (a) and (b) correspond to anguilliform and carangiform swimmers, respectively, at* Re *= 500, 1000, and 5000*

Additionally, Figure 11 presents data for time-averaged $C_D versus f^*$ for both swimming modes at the three values of Re. The negative values of $C_D$ corresponds to the generation of thrust here. In a way, certain combinations of Re $and\ f^*$, demonstrating $C_D \sim 0$, exhibit flow and kinematic parameters for self-propulsion or free-swimming conditions for the two kinds of swimmers. These critical points help identify flow-kinematic regimes where the swimmer can sustain motion without external force input, and they serve as physically meaningful benchmarks for comparing different swimmer styles and flow conditions. These critical points—where $C_D$

transitions from positive (drag-dominant) to negative (thrust-dominant)—serve as benchmark indicators**.** They allow us to identify the specific kinematic and flow conditions under which different kinematic types (e.g., anguilliform and carangiform) can sustain forward motion autonomously. Therefore, they are not just numerical values, but physically meaningful markers for understanding and comparing swimming efficiency, propulsion mechanisms, and the effectiveness of different undulatory styles.

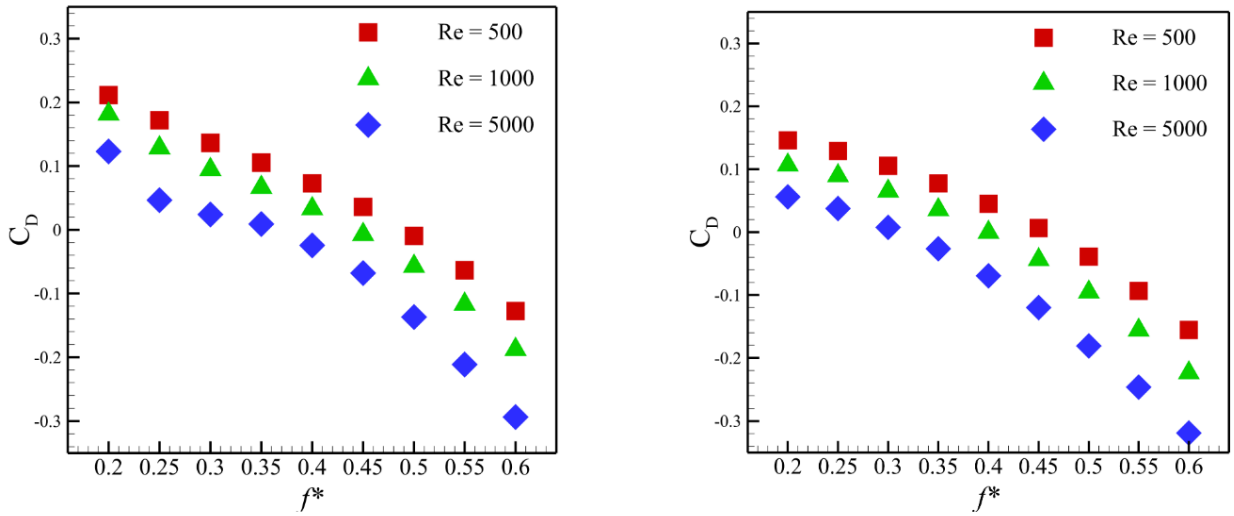


*Figure 11 Average drag coefficient values with different $f^*$ at Re = 500, 1000 and 5000 where (a) and (b) correspond to anguilliform and carangiform swimmers, respectively*

To understand the dependence of transport of odor on vortex dynamics around and in the wake of undulating bodies, there appears two direct routes: (i) we consider the vortex wake configurations through the classifications of von-Karman vortex street, neutral wake, and reverse von-Karman vortex street [5] and (ii) we carefully observe the classifications of the wake in terms of S, and P wakes, where S and P are the terms for a single vortex and a pair of vortices, respectively.

In unsteady flows generated by undulating swimmers, the structure of the wake—specifically how vortices are formed and shed—plays a critical role in influencing odor dispersion. Two common classifications used to describe wake patterns are 2S and 2P. The 2S wake pattern involves the shedding of one vortex per half oscillation cycle, meaning that over a full cycle, two single vortices are shed—one from each side of the swimmer. In contrast, the 2P wake pattern involves the shedding of a pair of counter-rotating vortices in each half cycle, leading to a more complex and energetic wake structure.

The later choice seems more viable, because our purpose here is not to connect the odor dynamics with the production of drag or thrust forces, but to explain the transport of chemical cues, apparently dependent on formation, shedding, and dynamics of vortices. Therefore, we adopt the second route to further explain our analysis. As evident from Figure 12a and Figure 12b, most of the parametric space corresponding to both anguilliform and carangiform swimmers consistently indicates the production of 2S wake, whereas only the anguilliform swimmer exhibits its wake transitioned to 2P patterns at Re = 5,000. This shift in wake structure suggests an increase in vortex interaction and fluid agitation, which likely leads to enhanced odor dispersion downstream. These observations emphasize the importance of wake topology in determining how effectively chemical cues are distributed in the swimmer's wake.

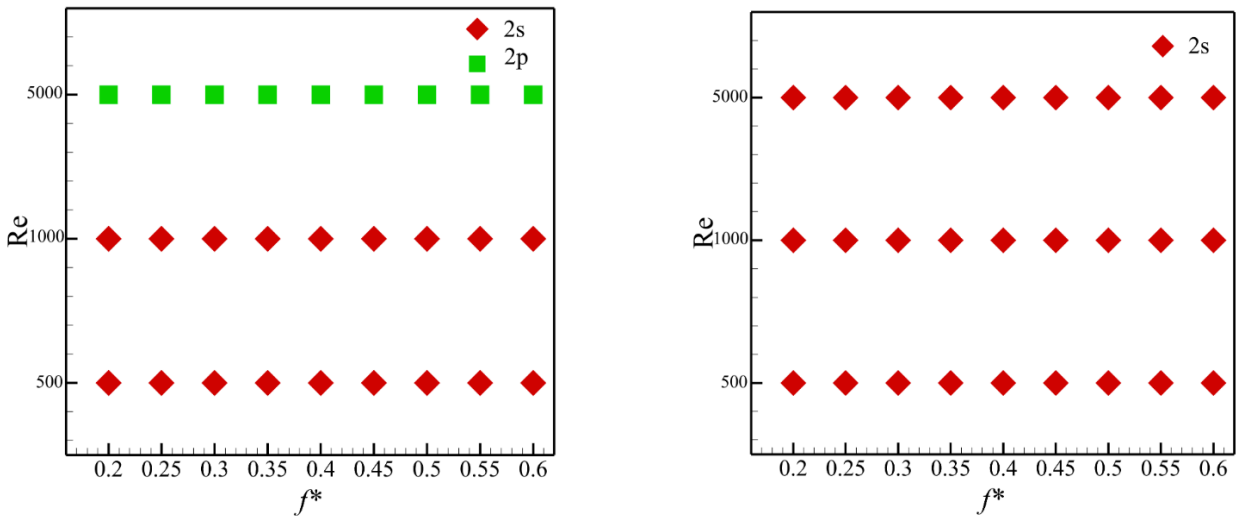


*Figure 12 Vortex configuration at Re = 500, 1000 and 5000 where (a) and (b) correspond to anguilliform and carangiform swimmers, respectively.*

Using the out-of-plane vorticity ($\omega_z$), we present these two distinct patterns of wakes in for Re = 5,000 and $f^*$= 0.2, observed at three time instants: $t/\tau = 0, t/\tau = 0.50, and\ t/\tau = 1.00$. The contour plots illustrate two distinct wake patterns. For the carangiform swimmer, a single dominant vortex is shed during each half of the oscillation cycle, consistent with the 2S classification. This pattern suggests a more streamlined and energy-conserving propulsion style, with minimal vortex interactions in the wake. In contrast, the anguilliform swimmer exhibits the formation and shedding of a pair of counter-rotating vortices during each half-cycle, corresponding to a 2P wake pattern. This more complex vortex structure indicates stronger fluid agitation and a greater degree of mixing in the wake. The annotations in Figure 13 highlight the placement and orientation of these vortices, making the difference in vortex shedding behavior between the two swimmer types visually and quantitatively apparent.

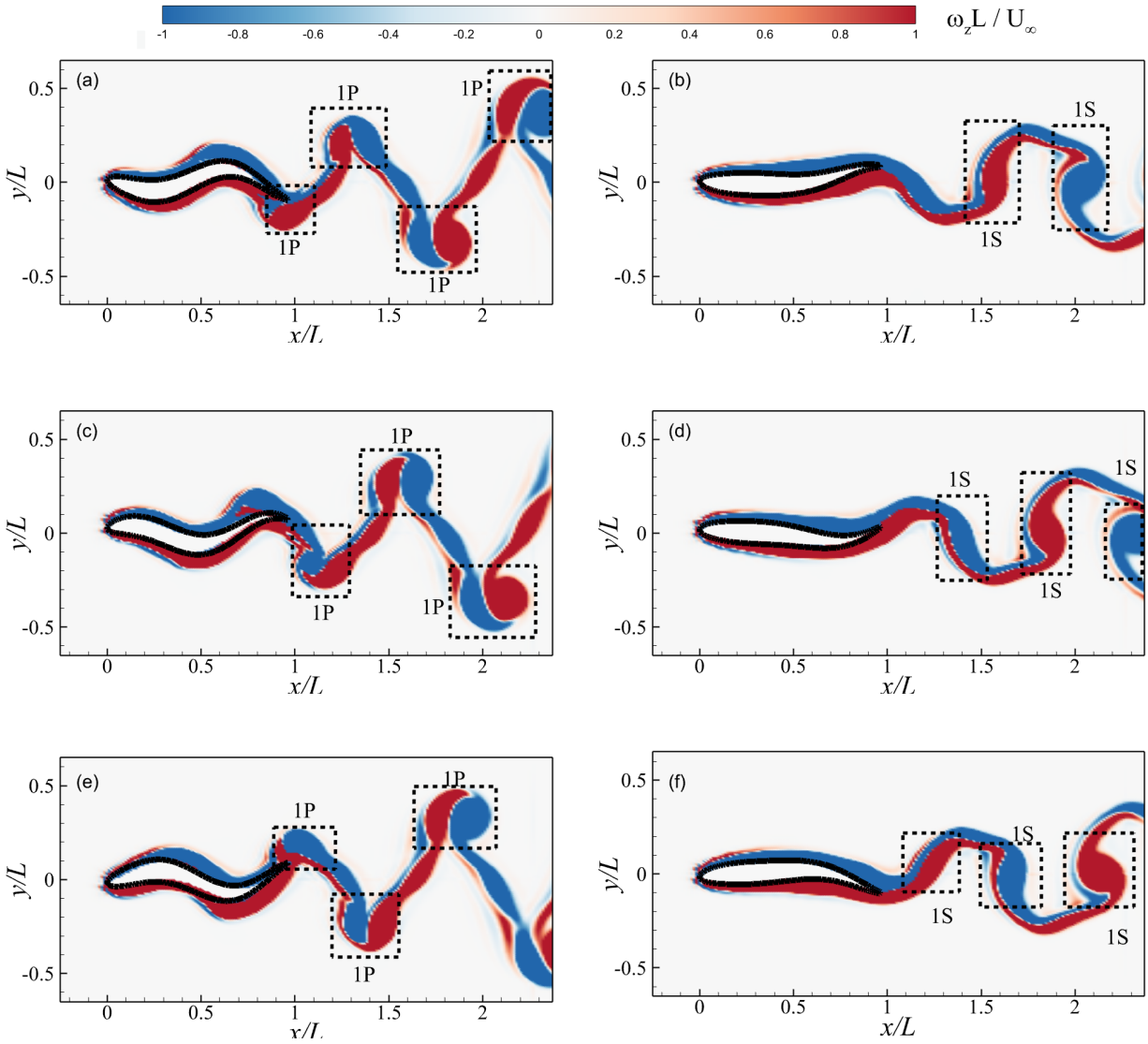


*Figure 13 Vortex configuration patterns at different time instants during the undulation cycle. The first row corresponds to $t/\tau$ = 0, the second row to $t/\tau$ = 0.50, and the third row to $t/\tau$ = 1.00. Panels (a), (c), and (e) show vortex patterns for anguilliform swimmers; panels (b), (d), and (f) for carangiform swimmers.*

- *Odor Transport Dynamics*

Because dynamics of the chemical cues are expected to be significantly influenced by the vortices generated by the undulating bodies, the next step is to investigate whether the distribution of odor follows the same patterns as the vortex dynamics. To explore their relation, we analyze flow and odor fields under various conditions according to the governing parameters in this study. Figure 14 and Figure 15 provides side-by-side comparative contour plots for the transport of vorticity and odor produced by anguilliform and carangiform swimmers, respectively. The plots in Figure 14a-Figure 14d and Figure 15a-Figure 15d represent the data for Re = 500 at $f^*$= 0.2 and $f^*$= 0.6. Similarly, the data presented in Figure 14e-Figure 14f and Figure 15e-Figure 15f correspond to Re = 5,000 at the same Strouhal frequencies. The first observation from the comparison of all the plots relates to the odor fields strongly linked with vortex dynamics in the wake. It is apparent that odor spots primarily seem to follow the trajectory of the vortices.

Another observation in the plots of Figure 14 and Figure 15 corresponds to strong odor spots quantified as the magnitude of $C^*$ for the higher $f^*$ for both Re. We find that odor is transported more strongly and to a farther distance in the wake of the undulating swimmers if they swim with a higher Strouhal frequency, irrespective of the Reynolds number. Based on the magnitude of $C^*$, a comparative look at the two sets of plots in Figure 14 and Figure 15 clearly indicate that the anguilliform swimmers is able to spread the odor more strongly to a farther distance in its wake, despite the fact that the carangiform swimmer undulates its body with a higher wave-speed.

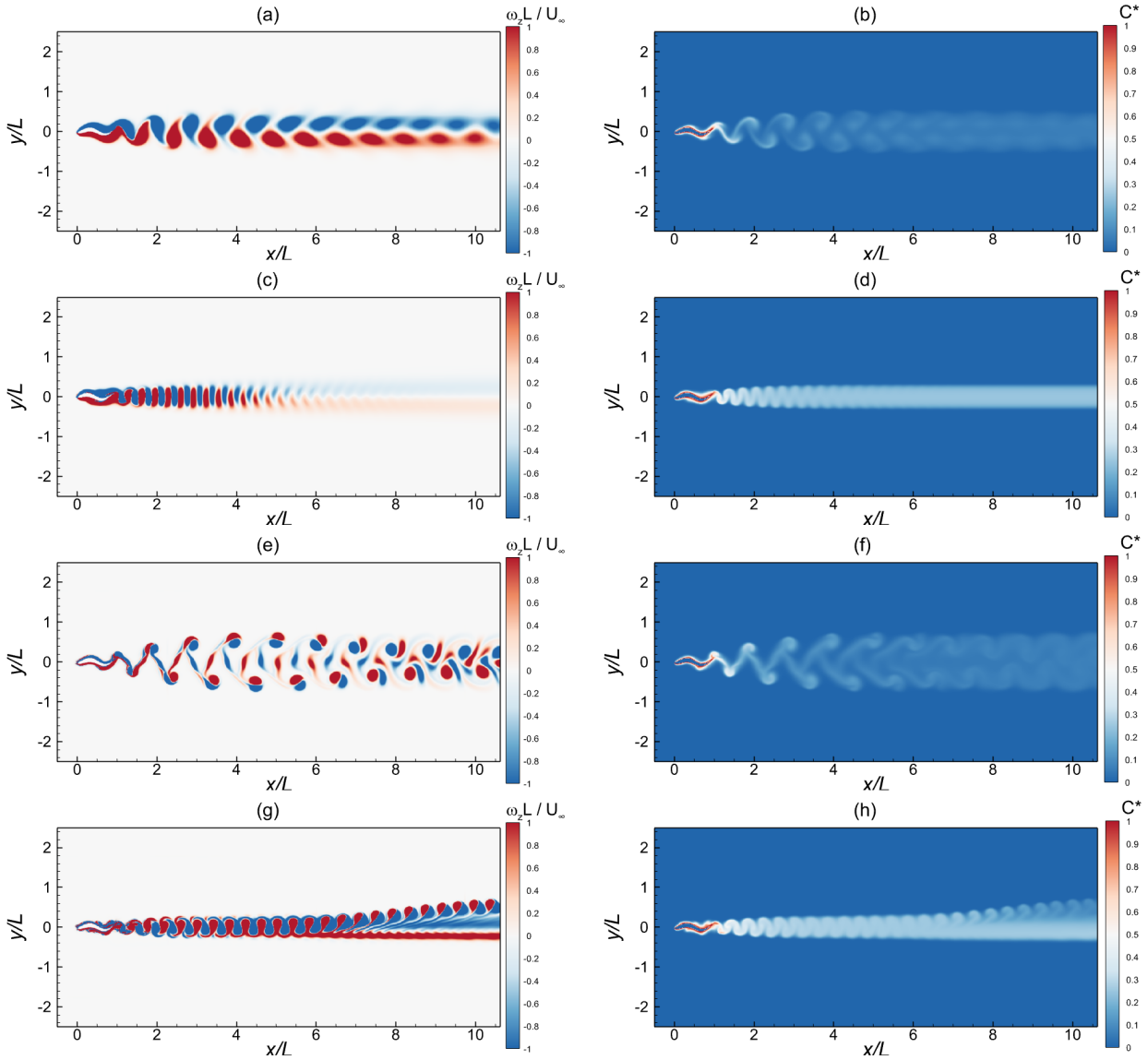


*Figure 14 Vortex and odor concentration for anguilliform swimmers, with the first and second columns corresponding to vorticity contours and odor concentration, respectively. Panels (a), (b) and (c), (d) display scenarios with a Re = 500 and $f^*$ = 0.2 and 0.6, respectively. Panels (e), (f) and (g), (h) display scenarios with a Re = 5000 and $f^*$ = 0.2 and 0.6, respectively.*

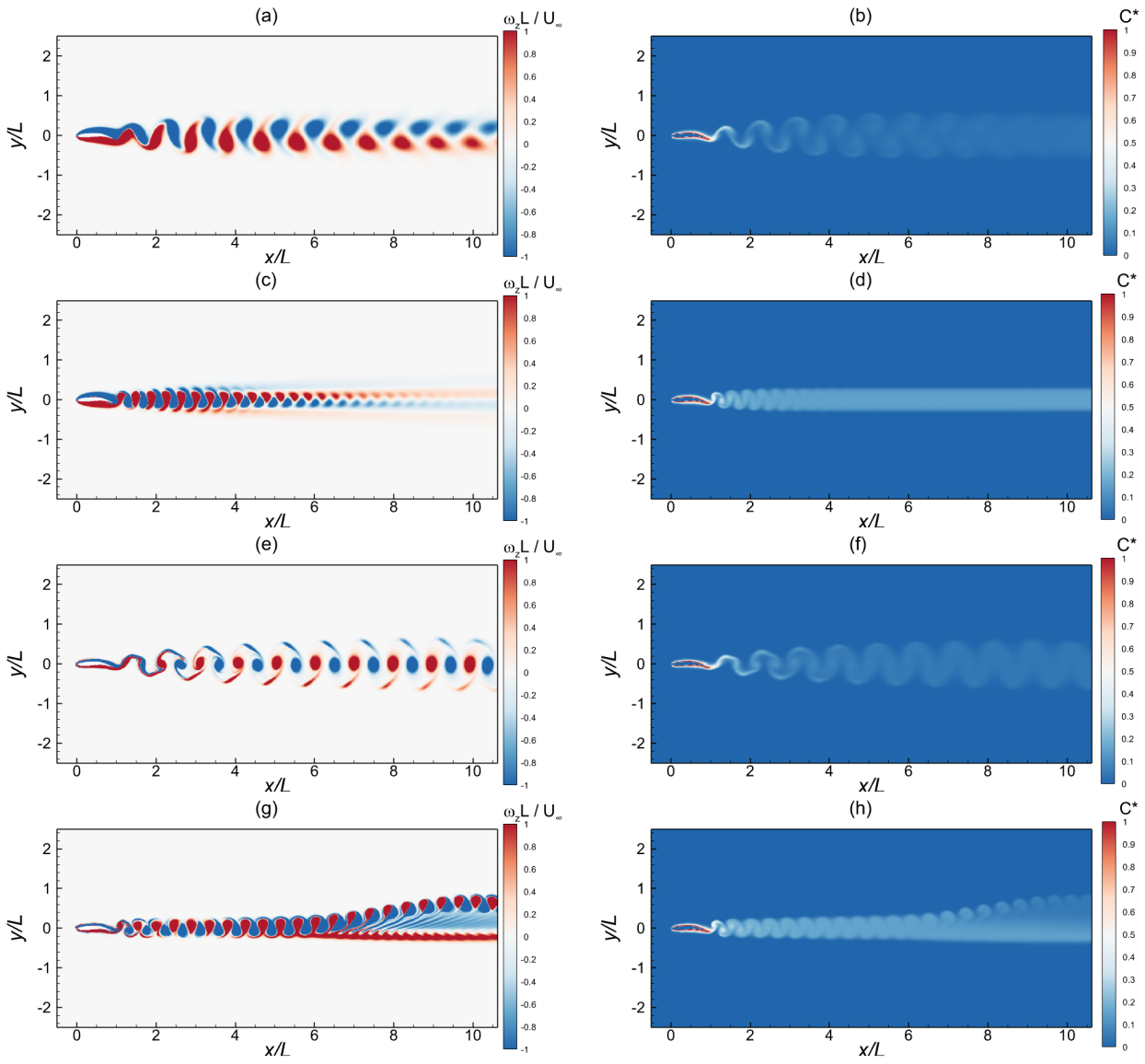


*Figure 15 Vortex and odor concentration for carangiform swimmers, with the first and second columns corresponding to vorticity contours and odor concentration, respectively. Panels (a), (b) and (c), (d) display scenarios with a Re = 500 and $f^*$ = 0.2 and 0.6, respectively. Panels (e), (f) and (g), (h) display scenarios with a Re = 5000 and $f^*$ = 0.2 and 0.6, respectively.*

After establishing a broad connectivity between odor and vorticity fields around the two undulating swimmers, the next important aspect is that how closely transport of chemical cues is linked with the dynamics of coherent flow structures.

To explore this aspect, we plot the contours of the two parameters, $\omega_z \; and \; C^*$, overlaid on each other in Figure 16a-Figure 16h. The plots of $C^*$ are shown in the form of solid black lines in all the cases here. It is evident that the not only the overall trajectory of the odor sports are driven by vortices, but also the periphery of the region with high vorticity is overlapped by that of the odor cues. Nevertheless, a careful look at inside the zones of higher activity of vorticity and odor transport in each case, the odor spots very rarely follow the exact paths of the vortices. It means that the odor spots are misaligned with the coherent flow features.

A better way to further analyze this behavior can be to plot the x- and y-coordinates of the centers of vortices and odor spots that is provided in Figure 17. Employing the methodology introduced and explained by Khalid et al. [3], we compute these coordinates (X, Y) of the centers of vortices and spots of odor through a local search to identify the locations of maximum and minimum vorticity and maximum odor concentration. In all the four cases presented here for different swimming modes and $f^*$ at Re=1,000, we do not observe a strongly linked local kinematics of chemical cues with either positive or negative vortices. The centers of the odor spots do not follow the cores of the vortices while traversing in the wake even when they are tracked to a distance of 10c from the trailing edge of the foil.

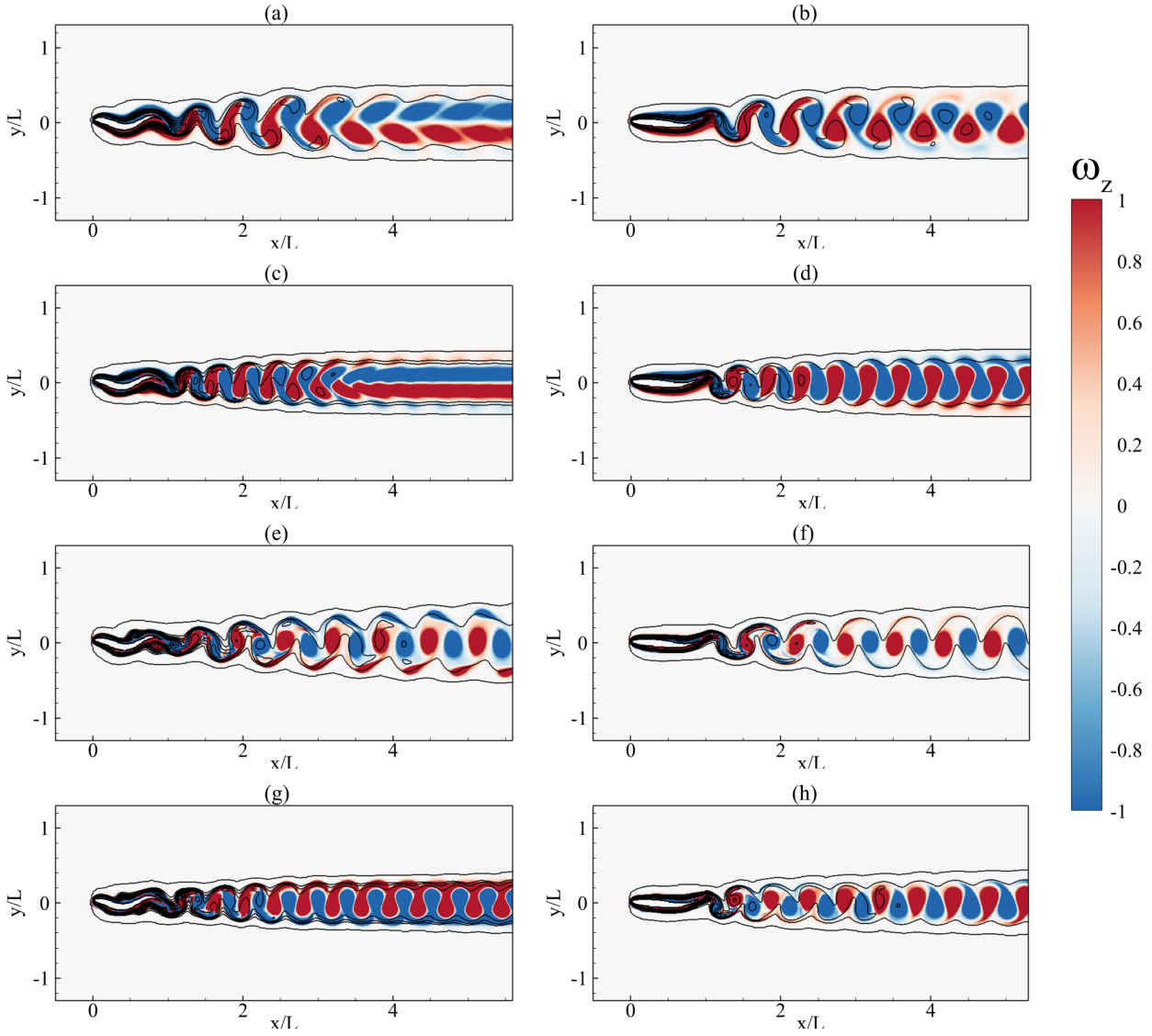


*Figure 16 Overlay plots for vorticity and odor concentration are presented for anguilliform and carangiform swimmers in the first and second columns, respectively. Panels (a), (b) and (c), (d) display scenarios with a Re = 1000 and $f^*$ = 0.3 and 0.5, respectively. Panels (e), (f) and (g), (h) display scenarios with a Re = 5000 and $f^*$ = 0.3 and 0.5, respectively.*

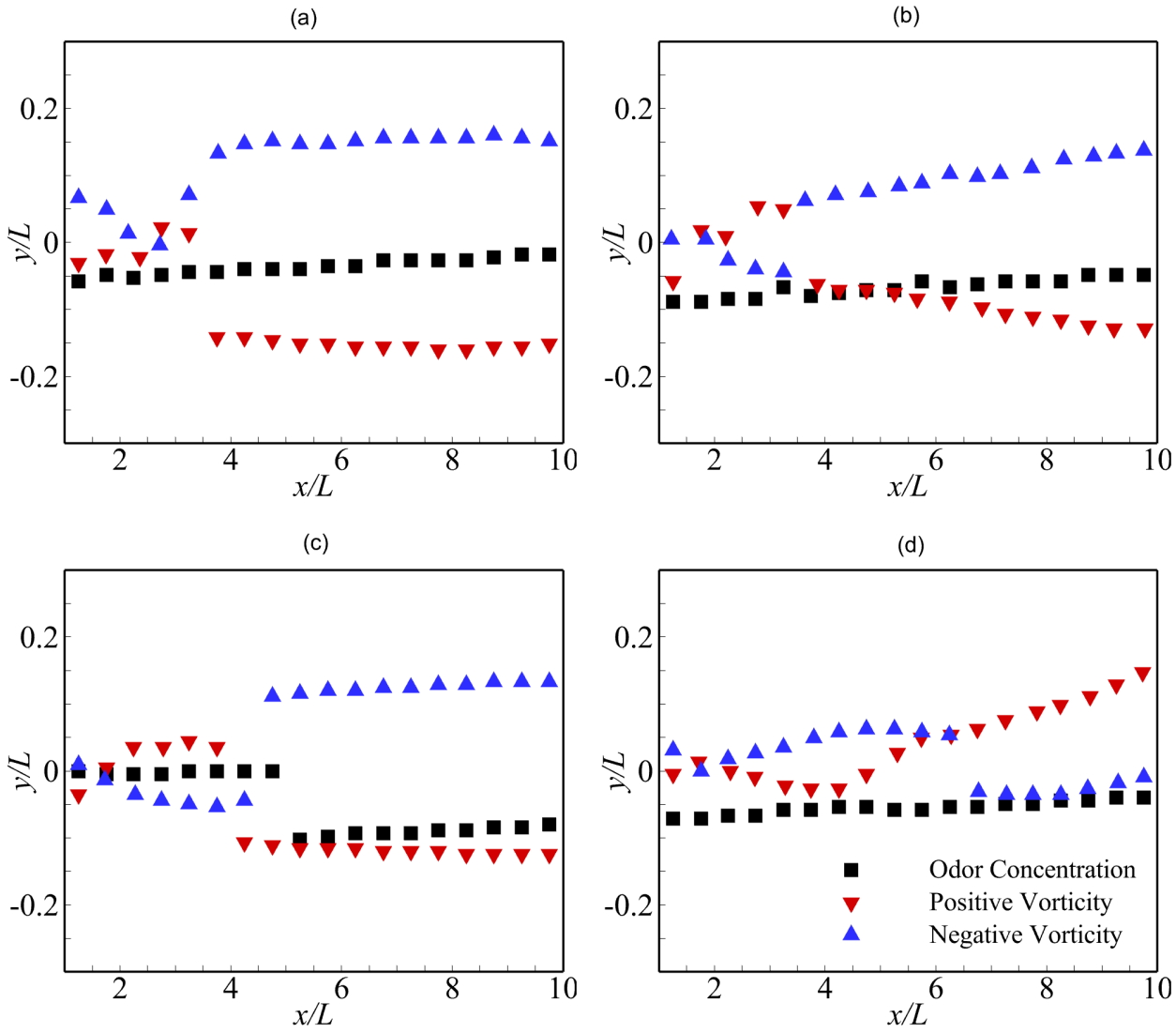


*Figure 17 Plot for coordinates of the center of vortices and odor spots for undulating swimmers are displayed in the first and second columns for anguilliform and carangiform swimmers, respectively. Panels (a) and (b) correspond to Re = 1000 and $f^* = 0.3$, while panels (c) and (d) correspond to $f^* = 0.5$*

- *Role of Convection and Diffusion in Odor Transport*

The next important element of this work is to determine the influence of convection and diffusion of chemical cues in the spread of odor in the wake. The interplay between diffusion and convection is of fundamental significance in shaping the dispersion and detection of chemical cues in aquatic environments.

To evaluate the relative influence of these two distinct phenomena on concentration and transport of odor, we employ the unsteady odorant advection-diffusion equation (Equation 3) to evaluate their individual contributions. For Sc = 340 for water, our observations from Figure 18 for the anguilliform swimmer and Figure 19 for the carangiform swimmer, identify that as the Reynolds number increases from 500 to 5,000, convection becomes increasingly dominant in spreading odorants, thereby enhancing the dispersion of chemical signals in the wake. This rise in the convective process improves the mixing and distribution of odor molecules, allowing for more effective and widespread detection of chemical signals far from the body. These observations do not seem to be influenced by the $f^*$ and the type of waveform imposed on the swimmer's body. The plots in the right-sided columns of Figure 18 and Figure 19 demonstrate that the diffusion process significantly diminishes with the increase of Re, but a higher $f^*$ slightly improves its strength in the wake.

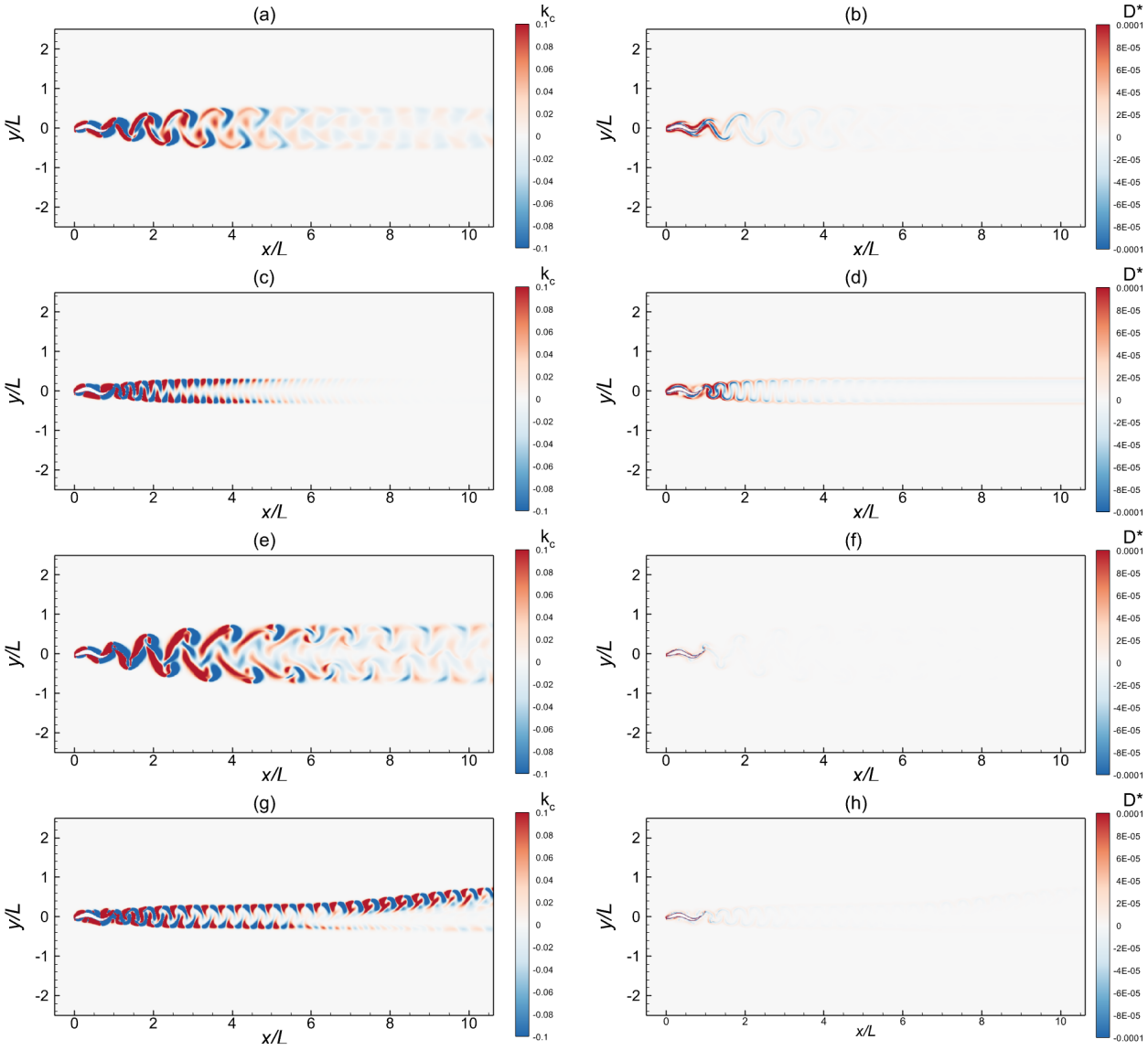


*Figure 18 Odor dynamics for anguilliform swimmers, with the first and second columns corresponding to convection and diffusion, respectively. Panels (a), (b) and (c), (d) display scenarios with a Re = 500 and $f^*$= 0.2 and 0.6, respectively. Panels (e), (f) and (g), (h) display scenarios with a Re = 5000 and $f^*$= 0.2 and 0.6, respectively.*

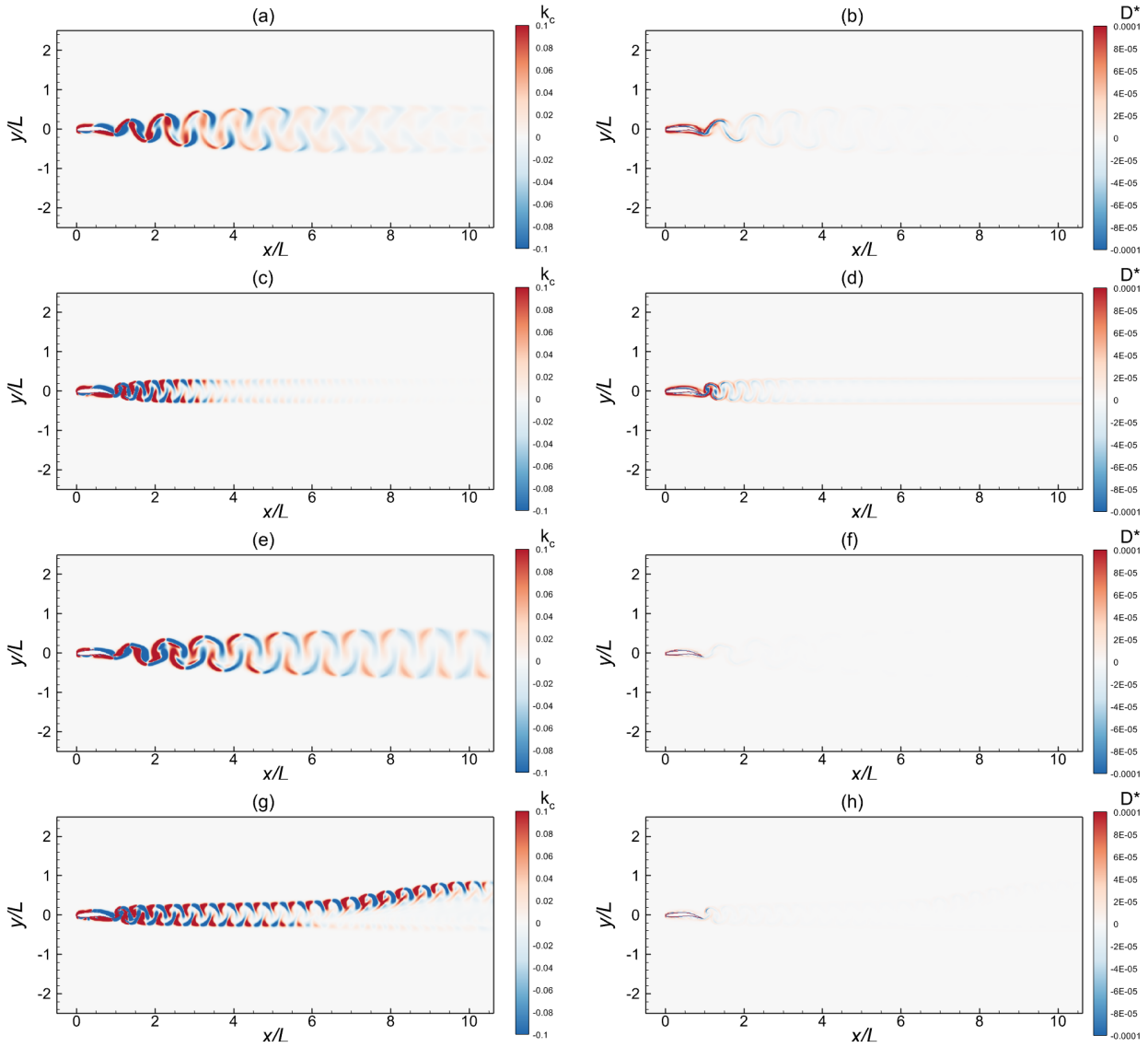


*Figure 19 Odor dynamics for carangiform swimmers, with the first and second columns corresponding to convection and diffusion, respectively. Panels (a), (b) and (c), (d) display scenarios with a Re = 500 and $f^*$ = 0.2 and 0.6, respectively. Panels (e), (f) and (g), (h) display scenarios with a Re = 5000 and $f^*$ = 0.2 and 0.6, respectively.*

Because most of the previous studies in literature [26], [27], [52] focused on the phenomenon relevant to Sc ranging up to 100, which does not correspond to the conditions in water, we make it an integral part of our present work due to the importance of fluid-structure-chemical interactions in marine environments. Although undulatory motion belongs more to fish species propelling in water, we test and demonstrate the robustness of our in-house solver by considering Sc for two media - water and air — to elaborate how convection and diffusion processes are impacted by the Schmidt number and how this parameter determines the dominance of one phenomenon over the other. For this purpose, we choose a transitional flow regime with $f^*$ of 0.45 for both undulating swimmers as representative cases in Figure 20. In aquatic environments like water, where the value Sc is high for water, convection predominantly drives the dispersion of chemical cues. The high density and viscosity of water enhance turbulent mixing, thereby promoting effective convective transport while diminishing the relative impact of molecular diffusion. Conversely, Sc decreases substantially in air due to its lower density and viscosity, making molecular diffusion more significant in odorant distributions, as illustrated in Figure 20. The reduced convective mixing in the air allows diffusion to play a more prominent role in the spread of chemical signals, leading to a more gradual and extensive dispersion pattern. We observed that in air, the impact of odor concentration is stronger due to the additional effect of diffusion. On the other hand, diffusion has a minimal effect on odor concentration in water, with convection being the primary mechanism for odor dispersion. Therefore, in aquatic environments, the spread of odor is primarily driven by convection, while in air, both convection and diffusion play significant roles, and contributions from none of them may be disregarded.

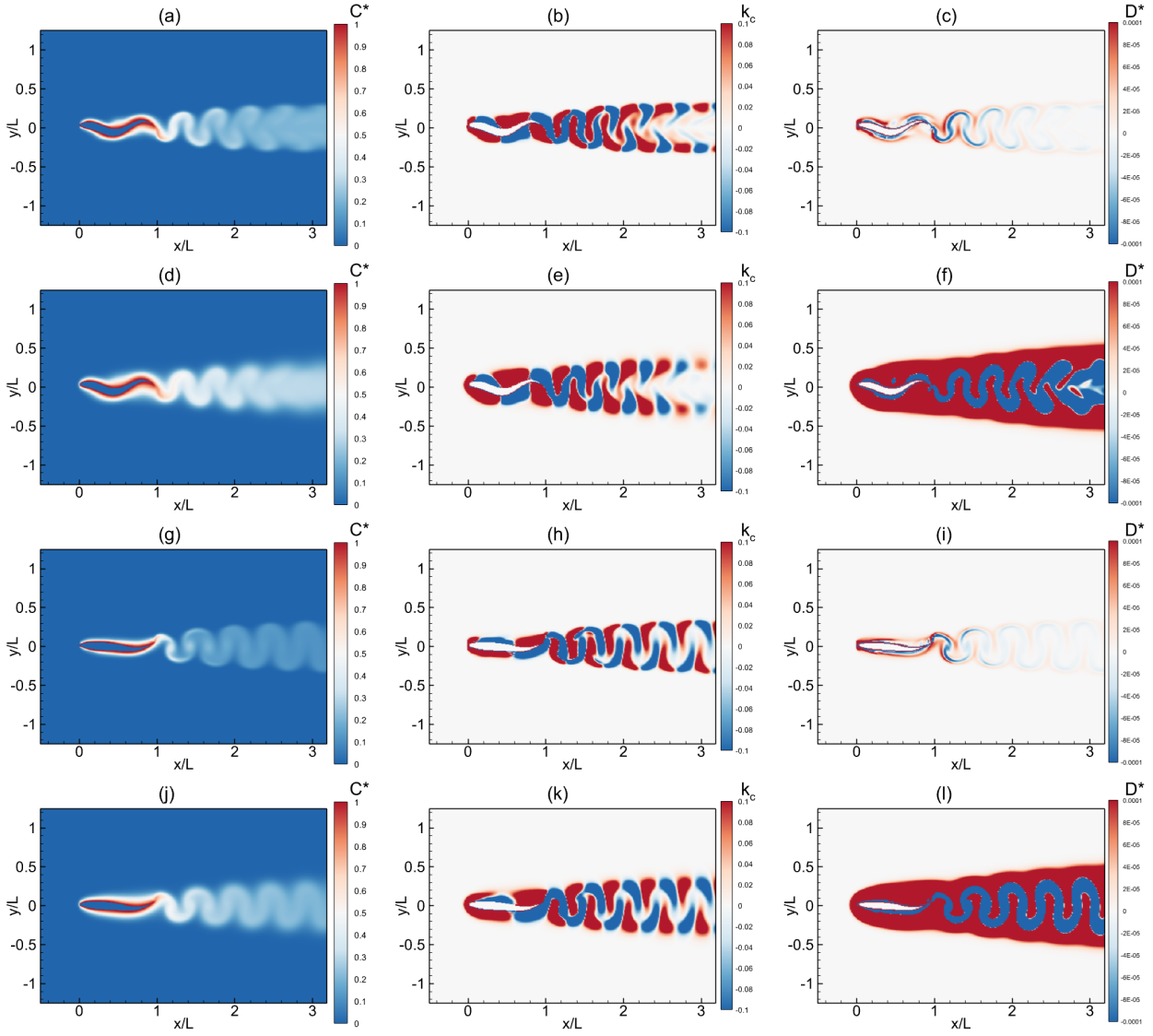


*Figure 20 Side-by-side comparison of odorant dynamics, focusing on concentration (first column), convection (second column), and diffusion (third column). Panels (a) through (f) and (g) through (l) represent anguilliform and carangiform swimmers, respectively. Panels (a) to (c) and (g) to (i) show water as the medium, while panels (d) to (f) and (j) to (l) depict air as the medium.*

In this chapter, we performed two-dimensional simulations to analyze the relationship between vortex formation and odor dispersion around undulating swimmers. Although odor fields are often associated with regions of high vorticity, their paths do not consistently align with coherent vortex structures, revealing a non-linear interaction. Anguilliform swimmers generated broader and more persistent odor trails compared to carangiform ones, especially at higher reduced frequencies. Convective transport was dominant in water due to high Schmidt numbers, while diffusion had a greater role in air. Reynolds and Strouhal numbers were found to critically influence odor transport dynamics.

# Chapter 4: Three-Dimensional Vortex-Odor Interaction for Solitary Fish

This chapter investigates the role of swimming kinematics and body morphology in the transport of chemical cues within the wake of solitary swimmers using high-fidelity three-dimensional simulations. By applying a sharp-interface immersed boundary method coupled with an odor transport model, we simulate carangiform and anguilliform motions, i.e., jackfish and eel geometries at a Reynolds number of 3000. Results show that odor plumes are strongly coupled with vortex structures, with kinematics—rather than morphology—being the primary driver of chemical dispersion. Anguilliform motion leads to broader and longer-lasting odor trails and increasing undulation amplitude further enhances odor spread due to stronger convective momentum transfer. These findings advance our understanding of underwater chemical sensing and offer practical insights for the design of autonomous underwater robots capable of efficient odor-based navigation.

- *Flow Configuration and Governing Parameters*

Extending our research from Two-Dimensional to Three-dimensional, we perform simulations of fluid flows and odor dynamics around 3D undulating bodies. The governing flow, kinematic, and odor-related parameters used in these simulations are summarized in Table 4. The simulations are conducted within a transitional flow regime [3], with two distinct waveform patterns, including anguilliform and carangiform, over the bodies of the two swimmers [49].

These waveforms are prescribed across a Strouhal number ($f^*$) = 0.25 and 0.40, consistent with the typical swimming patterns of marine animals [3]. For this study, we limit the governing parameters to those most relevant for 3D flows, as a detailed parametric analysis has already been performed and presented in our recent 2D study [49] (mentioned in Chapter 3: Two-Dimensional Vortex-Odor Interaction). It is worth noting that the undulation wavelength is set to $\lambda = 0.80$ for the anguilliform kinematic mode [7] and $\lambda = 1.05$ for the carangiform mode [5].

*Table 4 Specifications of governing parameters for 3D*

| Parameters | Specifications |
|---|---|
| Geometry | Eel and Jackfish |
| Undulatory kinematics | Anguilliform and Carangiform |
| Re | 3000 |
| Sc | 340 (water) |
| $f^*$ | 0.25 and 0.4 |
| $\lambda$ | 0.80 and 1.05 |

- *Coupled Vortex–Odor Dynamics*

We begin our discussion by presenting the vortex topology and odor dynamics around the jackfish with carangiform motion and the eel with anguilliform motion at Re = 3000 and $f^*$ = 0.40. For this purpose, we employ the Q-criterion to visualize 3D vortices [54]. The Q-criterion is defined as $\mathrm{Q} = 0.5(|\Omega|^2 - |\boldsymbol{S}|^2)$, where $\Omega$ represents the antisymmetric part and **S** represents the symmetric part of the velocity gradient tensor. Regions with Q > 0, where the rotation rate dominates the strain rate, indicate distinct coherent vortices. This tool enables us to identify different vortical structures around the body and in the wake.

Figure 21 shows the Q-criterion, visualized in light grey with a value of 10, alongside the non-dimensional odor concentration ($C^*$) at three levels: $C^*$= 0.8 (blue), $C^*$ = 0.6 (purple), and

$C^*$ = 0.4 (pink). Here, the swimmer's body serves as the source, where $C^*$ = 1. Two key observations emerge from these plots in Figure 21. First, the odor plumes not only strictly follow the vortex topology but also reside within it, indicating a strong coupling between the flow structures and odor transport. Second, the Eel with anguilliform kinematics produces stronger and farther-reaching odor plumes compared to the Jackfish with carangiform kinematics. These findings align with the results of Kamran et al.[49], with one notable exception. The overall trajectory of odor spots and coherent flow structures were not always precisely aligned in our previously reported 2D simulations, and a phase shift between the two fields was evident. This phase shift is absent in our current work as it incorporates 3D effects, which capture more complex interactions between odor dynamics and vortical structures.

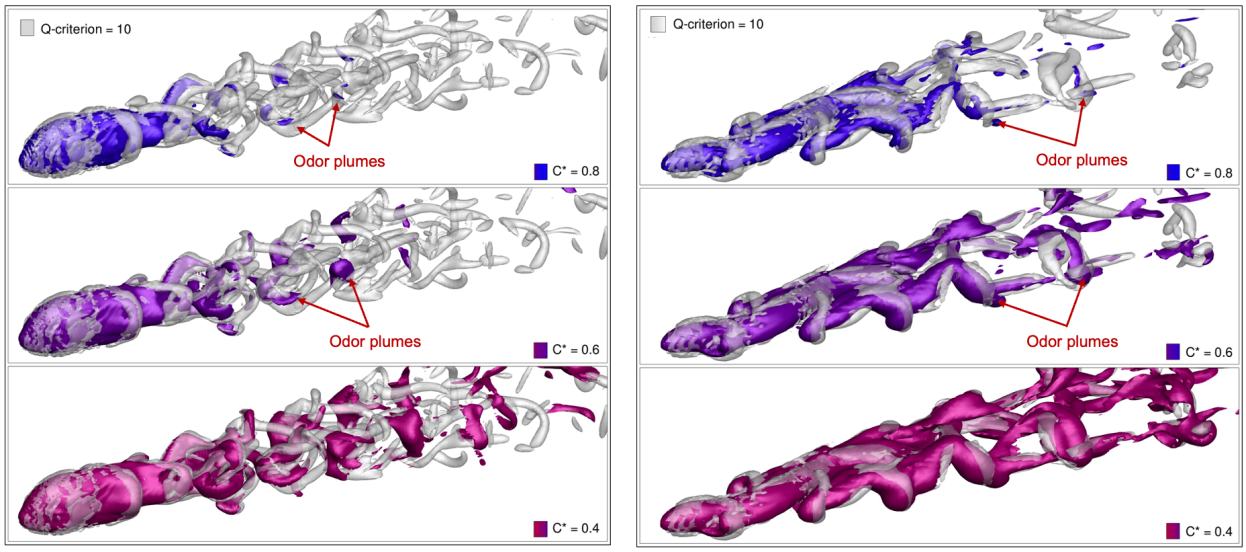


*Figure 21 Vortex topology visualized using the Q-criterion with a value of 10, at three different Odor concentration levels. The simulations are performed at Re = 3000 and $f^* = 0.4$. The first and second columns represent the results for jackfish (carangiform) and eel (anguilliform) swimmers, respectively.*

To further analyze this behavior, we quantify the results presented in Figure 22. We divide the wake region, starting from the trailing edge, into 10 subzones, each with a length of 0.5L, thereby covering the total wake region up to 5.5L downstream of the swimmer. For this analysis, we extract the isosurface of odor concentration at $C^*$ = 0.5, as concentrations below this threshold do not fall within the odor detection limit and have a significantly reduced effect. Data is collected at eight timesteps per oscillation cycle, and time-averaged, with the areas of the extracted isosurfaces of odor, normalized by the swimmer's body area. This normalization allows for a direct comparison of how effectively the odor is dispersed in their wakes by the two swimmers with different undulating kinematics. The normalized odor effectiveness is mathematically defined as:

$$C^*_{eff} = \frac{A_{iso}}{A_{fish}} (3)$$

where $A_{iso}$ is the isosurface area of odor within a given subzone, and $A_{fish}$ is the swimmer's body area.

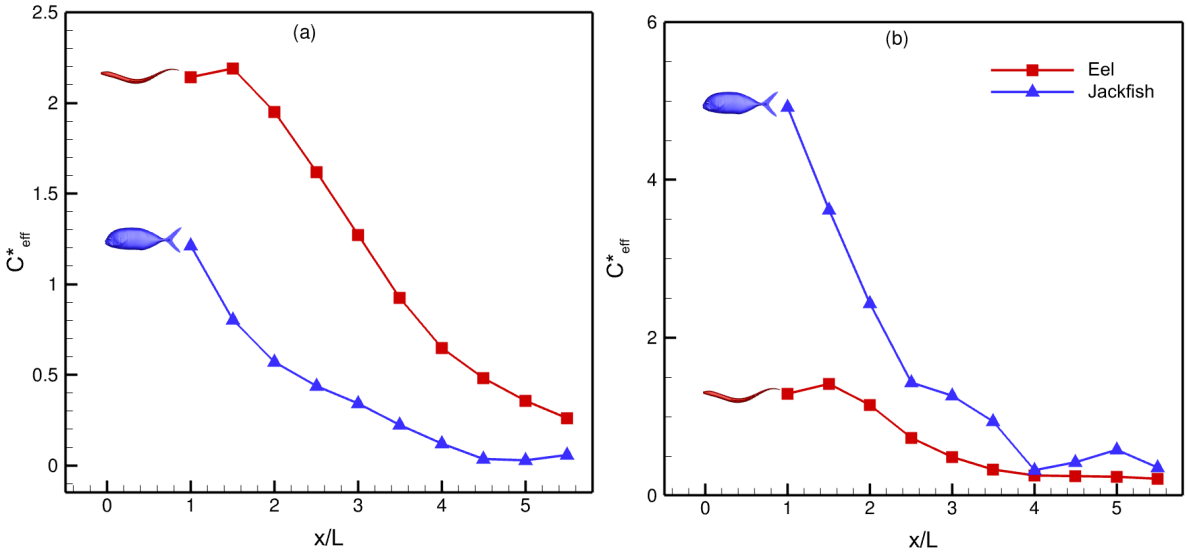


*Figure 22 Odor effectiveness in the wake of Jackfish and Eel: (a) actual and (b) opposite kinematics*

From Figure 22a and the observations from Figure 21, we note that $C^*_{eff}$ for the eel with anguilliform kinematics is significantly higher than that of the jackfish. Although the odor source area of the Jackfish is larger than that of the Eel, implying a potentially higher odor concentration in its wake, our results contradict this intuition. This discrepancy raises the question: why does the Eel produce a more effective odor plume despite having a smaller source area? To address this, we run additional simulations in which the kinematics are swapped between the two swimmers, assigning anguilliform kinematics to the Jackfish and carangiform kinematics to the Eel. Following the same procedure to compute $C^*_{eff}$, the results are plotted in Figure 22b. These findings clarify that it is not the swimmer's physiology, but rather its kinematics, that play a dominant role in spreading odor in the wake that is an important insight for underwater sensing techniques.

To further strengthen our argument, we address another key research question: how do kinematics influence decay of odor in the wake? To investigate this, we perform additional simulations by varying the magnification of undulation by $\pm 50\%$. Specifically, we adjust the amplitude profile for each swimmer's kinematics by scaling the amplitude equations for carangiform motion (Equation.4) and anguilliform motion (Equation.5) to achieve the desired magnification. The modified amplitude profiles are obtained by multiplying the original equations by scaling factors of A = 0.5 (50% decrease in magnification) and A = 1.5 (50% increase in magnification), while A = 1.0 represents the original undulation. Figure 22 exhibits the resulting odor concentration isosurfaces at C* = 0.5 for the undulatory swimmers, Jackfish and Eel, at these three levels of amplitude magnification.

We observe that as the amplitude magnification increases from A = 0.5 to A = 1.5, the odor concentration becomes more intensified, indicating that vortex activity diminishes odor dispersion in the wake. This behavior is also evident in Figure 21. To quantify this effect, we compute $C^*_{eff}$ for different magnifications of undulation, as shown in Figure 24. The results demonstrate that the odor effectiveness for the Eel (Figure 24b) is nearly twice that of the Jackfish (Figure 24a).

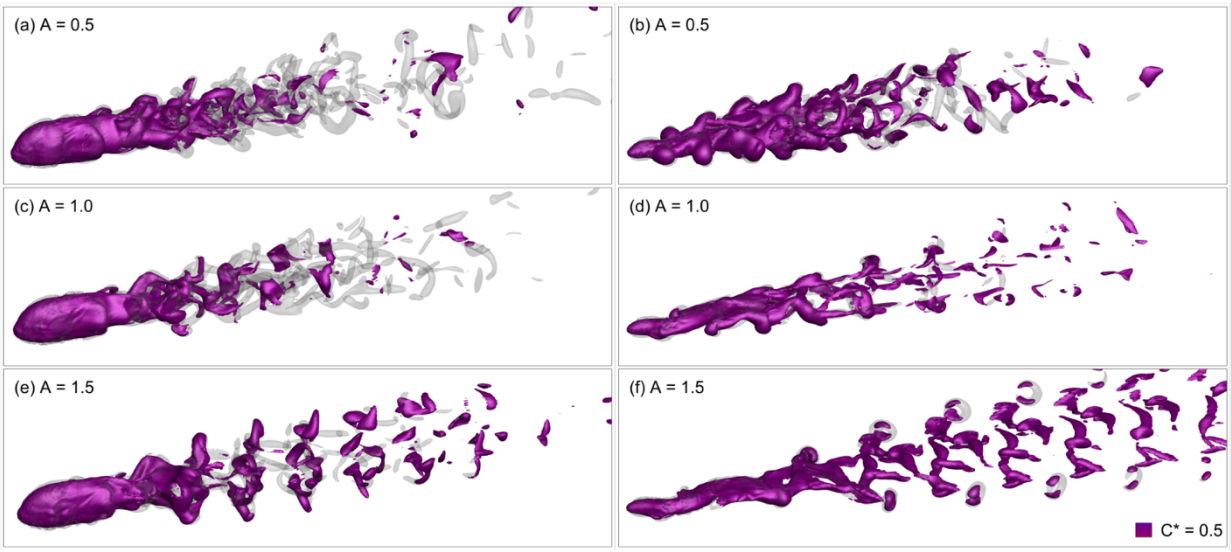


*Figure 23 Odor plumes for jackfish (first column) and eel (second column) with a different magnification of undulation*

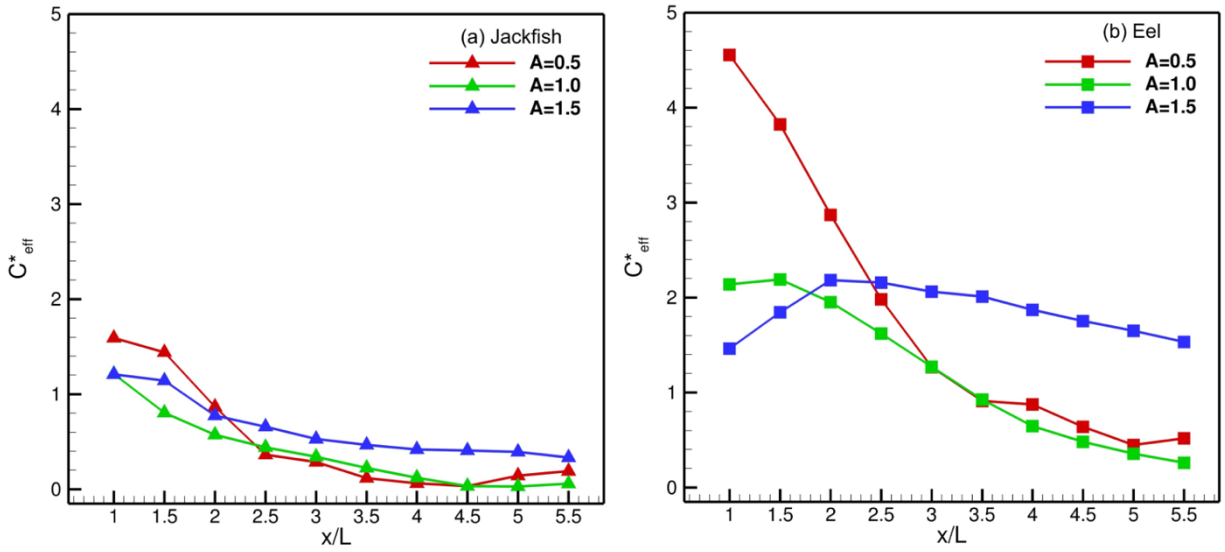


*Figure 24 Odor effectiveness with a different magnification of undulation: (a) Jackfish and (b) Eel*

Additionally, as seen in Figure 23 and Figure 24, the odor concentration tends to settle within a region up to 2.5L downstream. The differences in undulation patterns between the two swimmers further highlight the observed trends. For the Jackfish, where undulation is primarily concentrated in the posterior region (mainly the tail), the odor effectiveness decreases exponentially in the wake. In contrast, for the Eel, which exhibits undulation along its entire body, the maximum odor effectiveness at A = 0.5 and A = 1.0 follows an exponential decay, whereas at A = 1.5, the decay starts occurring at a farther downstream location, approximately at a distance of 2L from the swimmer. Finally, for both swimmers, the maximum odor effectiveness is observed at A = 1.5. This is because the increased magnification of undulation amplitude leads to greater work done on the surrounding fluid, thereby increasing momentum transfer and enhancing odor transport in the wake.

- *Role of Convection and Diffusion in Odor Transport*

An important aspect of this study is to determine the influence of convection and diffusion components on the transport of chemical cues in the wake[49]. To evaluate these effects individually, we discretize the advection-diffusion equation (Equation.3) and analyze the contributions of the convection and diffusion terms separately. The convection term (the second term on the left-hand side) is discretized using a QUICK scheme to ensure stability in the presence of advection-dominated flows, while the diffusion term (on the right-hand side) is discretized using the Crank-Nicolson scheme to capture the finer gradients of diffusive transport accurately. To gain a more detailed understanding of these mechanisms, we plot top views and z-axis slices (mid planes) of the flow field for both convection and diffusion, as shown in Figure 25 and Figure 26.

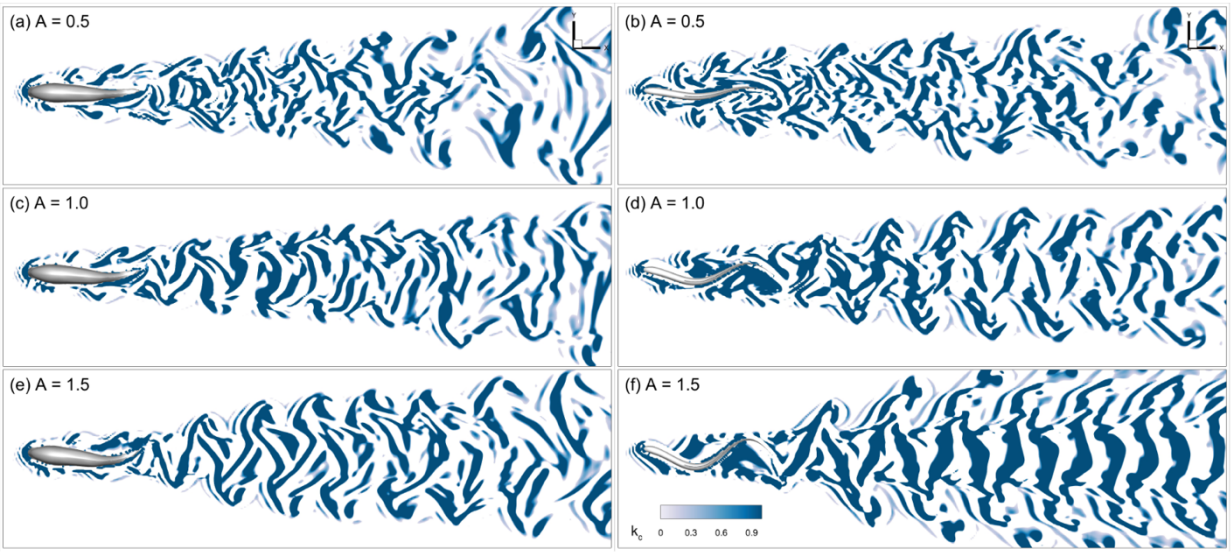


*Figure 25 Influence of convection for Jackfish (first column) and Eel (second column) with a different magnification of undulation*

At a 50% increased magnification of undulation (A = 1.5), convection ($k_c$) significantly dominates the wake dynamics for both the Jackfish and Eel, leading to an intensified odor concentration in the downstream region. The amplified motion results in higher momentum transfer to the surrounding fluid, which in turn accelerates the convective transport of odor. This observation aligns with the results in Figure 25 and Figure 26, where the stronger undulatory motion enhances odor transport in the wake. In contrast, at a lower undulation magnitude (A = 0.5), the reduced body motion leads to lower momentum transfer to the surrounding fluid. As a result, convection plays a less dominant role, and diffusion ($D^*$) becomes more significant, particularly in the crossflow direction. It means that instead of being advected efficiently downstream, the odor disperses more laterally due to molecular diffusion. This diffusive transport causes the chemical cues to spread transversely rather than forming a concentrated wake structure, leading to a lower net odor transport in the downstream direction.

A noteworthy observation is that while diffusion plays a role in transverse dispersion, its overall effect is minimal compared to convection. It is primarily due to the high Schmidt number (Sc) for water, which indicates that the relative importance of molecular diffusion is much smaller than that of convection in aquatic environments. Consequently, the primary transport mechanism for odor in the wake of undulating swimmers is dominated by convective processes, especially at higher undulation amplitudes, while diffusion provides a secondary effect, primarily contributing to the lateral spread of odor.

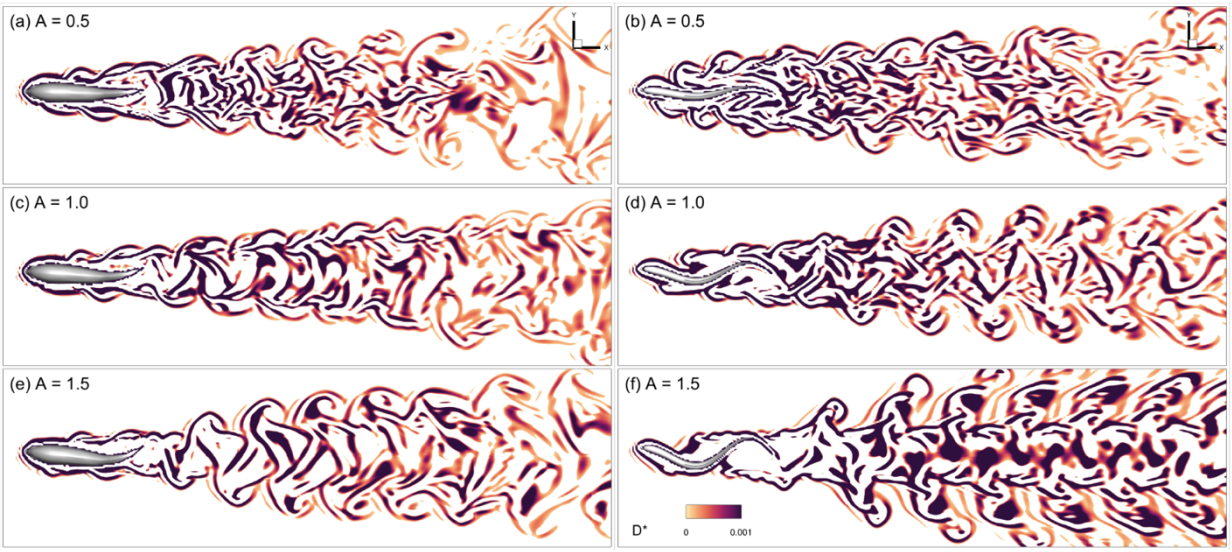


*Figure 26 Influence of diffusion for Jackfish (first column) and Eel (second column) with a different magnification of undulation*

This chapter presents a detailed analysis of three-dimensional odor transport in the wake of undulatory swimmers, focusing on the effects of kinematics and morphology. Through simulations of carangiform and anguilliform motions in jackfish and eel models, we show that swimming kinematics are the dominant factor influencing chemical cue dispersion, while morphological differences play a lesser role. Kinematic-swapping experiments reinforce this conclusion, with the odor distribution pattern following the imposed motion profile rather than the body shape. Enhanced undulation amplitude results in greater momentum transfer and more effective odor propagation. The odor field remains closely aligned with vortex structures, highlighting the dominance of convective transport over diffusion.

# Chapter 5: Three-Dimensional Vortex-Odor Interaction for Fish Schooling

This chapter investigates the collective effect of fish schooling on odor dispersion using three-dimensional computational fluid dynamics simulations. Multiple swimmers, modeled with anguilliform and carangiform kinematics, are analyzed across four schooling configurations: Mono-Fish, Bi-Fish, Tri-Fish, and Quad-Fish. The Q-criterion is used to visualize vortex structures alongside iso-surfaces of odor concentration. Results show that increasing the number of swimmers enhances lateral odor dispersion, while downstream propagation remains relatively unchanged beyond a spacing threshold. Quantitative analysis of normalized odor effectiveness indicates a linear increase in odor strength with the number of swimmers at any wake location.

- *Flow Configuration and Governing Parameters*

We extend our research evolution from 3D solitary fish to multiple fish, commonly referred to as fish schooling. The simulations take place within a transitional flow regime at a Reynolds number (Re) of 3000 [3], with two distinct undulating waveform patterns: anguilliform and carangiform, applied to the bodies of the two swimmers[49]. These waveforms are prescribed for $f^*$ = 0.40, consistent with the typical swimming patterns of marine animals. It is important to note that the undulation wavelength is set to $\lambda/L = 0.80$ for the anguilliform kinematic mode [7]and $\lambda/L = 1.05$ for the carangiform mode [5].

- *Coupled Vortex–Odor Dynamics*

We begin our discussion by presenting the vortex topology and odor dynamics around the eel with anguilliform motion and the jackfish with carangiform motion Re = 3000 and $f^*$ = 0.40 in four different configurations. For this purpose, we employ the Q-criterion to visualize 3D vortices[54]. Figure 27 and Figure 28 show the Q-criterion, visualized in light gray with a value of 10, alongside the non-dimensional odor concentration (C*) at C* = 0.5 (pink). The swimmer's body acts as the source, where C* = 1.

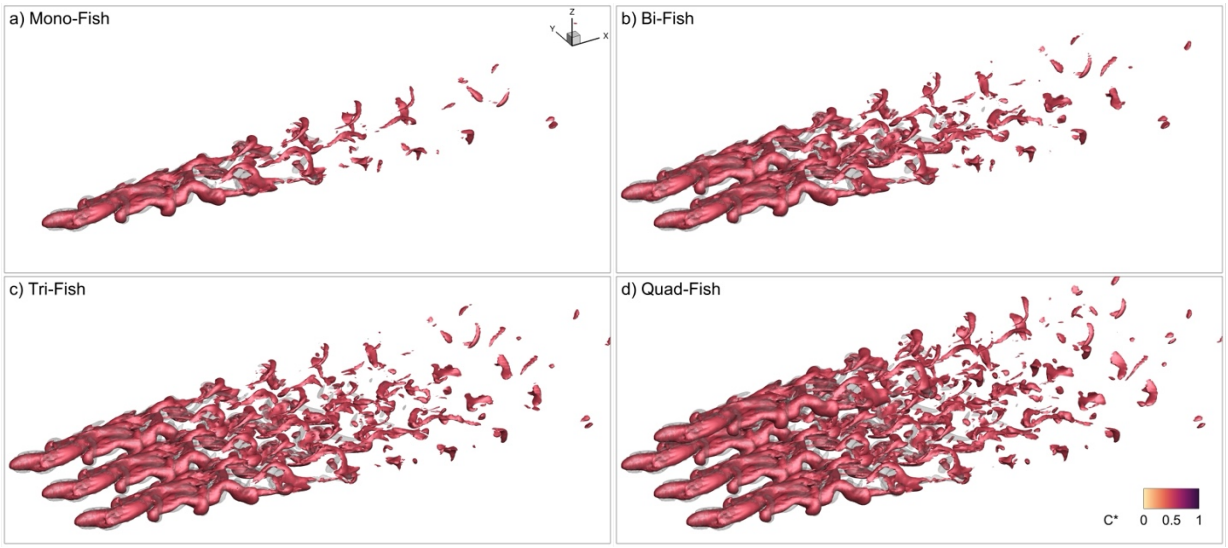


*Figure 27 Vortex topology visualized using the Q-criterion with a value of 10, and odor concentration level at 0.5 for different configurations of eel*

From Figure 27, we observe that as the configuration transitions from Mono-Fish to Quad-Fish, odor plumes in the lateral direction produce a stronger effect. However, in the downstream region, the odor dispersion does not have a significant effect, regardless of whether it is a Mono-Fish, Bi-Fish, Tri-Fish, or Quad-Fish, despite each configuration having a greater number of odor sources than the previous one. Similar results are observed for the jackfish in Figure 28.

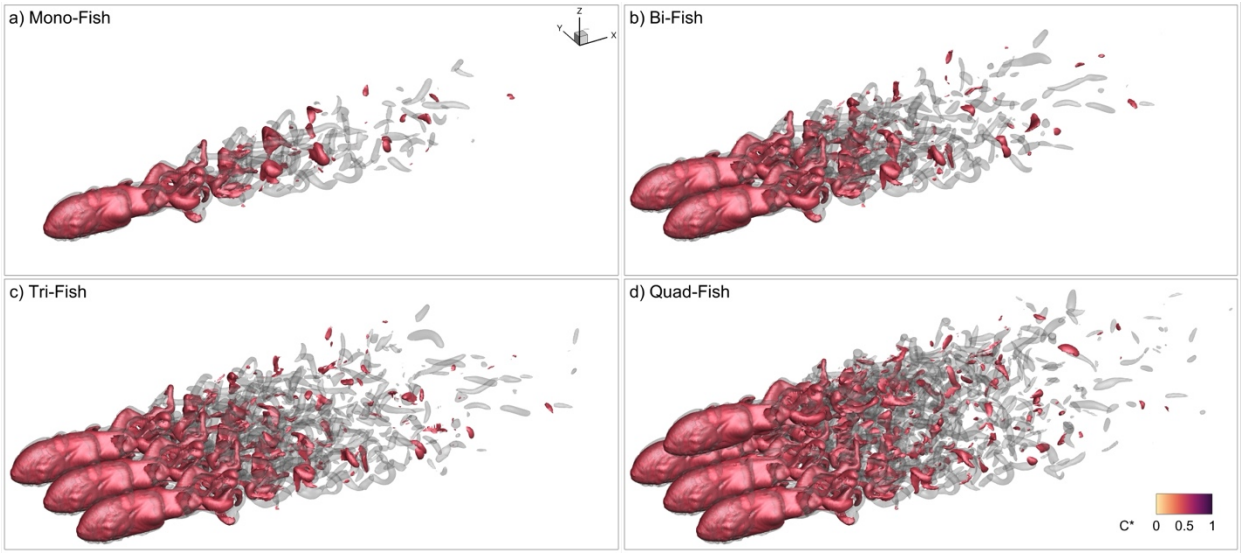


*Figure 28 Vortex topology visualized using the Q-criterion with a value of 10, and odor concentration level at 0.5 for different configurations of jackfish*

To further analyze this behavior, we quantify the results presented in Figure 29. We use the same methodology as mentioned in Chapter 4: Three-Dimensional Vortex-Odor Interaction. to quantify the results by calculating the normalized odor effectiveness.

It is important to note that we normalize by the swimmer's body area $(A_{fish})$, specifically using the area of the Mono-Fish, to ensure consistent quantification. From Figure 29a–b, we observe that $C^*_{eff}$ for the eel and jackfish increases linearly. Additionally, from Figure 29b, we note that for the jackfish, after 3.5L, the influence of fish schooling becomes equivalent to that of an individual fish. These findings clarify that for fish schooling configurations, the strength of odor increases linearly with the number of fish at any location in the wake.

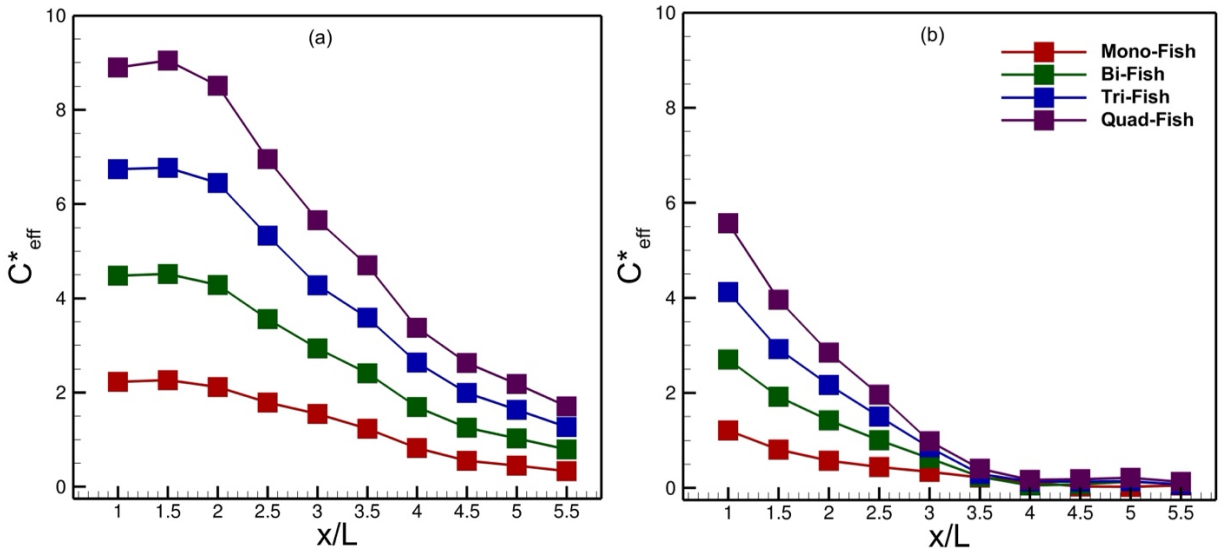


*Figure 29 Odor effectiveness in the wake of (a) an eel and (b) jackfish*

In this chapter, we explored the influence of fish schooling on odor transport through high-fidelity 3D simulations involving multiple undulating swimmers. As the number of swimmers increased, lateral dispersion of the odor field was significantly amplified, whereas downstream propagation reached a saturation point beyond a certain distance. Quantitative results showed a consistent linear increase in odor signal strength across all wake locations with each added swimmer. Notably, for carangiform swimmers, the contribution of additional swimmers beyond 3.5 body lengths became negligible in the downstream region.

# Conclusions

This research began with a two-dimensional analysis of odor transport and its interaction with vortex dynamics around undulating swimmers, specifically comparing carangiform and anguilliform kinematic modes. Through these simulations, we observed that while odor fields often overlap with regions of high vorticity, they do not consistently follow vortex paths or align with vortex cores, revealing a complex, non-linear relationship between odor dispersion and vortex structures. Our results showed that at higher reduced frequencies ($f^*$), odor is carried further downstream, with anguilliform swimmers achieving more effective dispersion due to their larger undulation amplitudes. Flow parameters such as Reynolds and Strouhal numbers were also found to significantly impact transport dynamics, where higher values enhanced convective transport. Importantly, we observed that in water—due to its higher Schmidt number—convection dominated odor dispersion, whereas in air, diffusion played a more prominent role, resulting in broader and slower-spreading odor plumes. Although limited to two-dimensional flows and moderate Reynolds numbers, this stage of the work provided foundational insights into the interplay between fluid dynamics and chemosensory transport.

Building upon the 2D findings, we extended our investigation to three-dimensional simulations using real geometric models of biological swimmers: the anguilliform Eel and the carangiform Jackfish. These high-fidelity simulations allowed us to analyze both the hydrodynamic and chemical wake structures in more realistic settings. Our results demonstrated that it is the swimmer's kinematics—rather than body morphology—that primarily dictate the structure and persistence of odor plumes. Kinematic-swapping experiments, where the motion patterns were exchanged between the two geometries, confirmed that the swimming motion

governs chemical dispersion. We also found that increasing undulation amplitude leads to greater momentum transfer into the fluid, resulting in more effective odor transport. These findings not only validate our earlier 2D observations but also emphasize the dominant role of convection in aquatic odor dispersion. This understanding directly informs the design of underwater robotic systems capable of enhanced chemical sensing and navigation.

Finally, we expanded our study to explore fish schooling and its collective effect on odor transport. By simulating multiple swimmers in formation, we discovered that adding more swimmers increased lateral spreading of odor, while downstream propagation remained relatively constant beyond a certain spacing threshold. A key observation was the linear increase in odor signal strength with the number of swimmers, at any location in the wake. Overall, our research bridges the gap between vortex dynamics and chemical transport across multiple scales, offering new directions for bio-inspired propulsion, sensory modeling, and robotic applications in complex aquatic settings.

# Future Recommendations

The following directions are recommended for future research based on this study:

- **High Reynolds Number Simulations**: Future work should perform simulations at higher Reynolds numbers to better capture turbulent effects and understand odor transport under more realistic aquatic conditions.
- **Experimental Validation**: Physical experiments are recommended to validate the computational models developed in this study, helping to improve the accuracy and reliability of odor dispersion predictions.
- **Broader Swimming Mode Analysis**: In addition to the carangiform and anguilliform modes explored here, future studies should consider sub-carangiform, thunniform, and ostraciiform swimming to provide a more holistic view of how propulsion mechanics affect fluid-odor interactions.
- **Impact of Kinematic Variations**: Further analysis is needed to understand how variations in undulatory kinematics influence odor plume formation and dispersion across different swimming strategies.
- **Applications in Bio-Inspired Robotics**: Insights from these extended investigations can inform the development of underwater robots capable of efficient chemical plume tracking, contributing to advancements in bio-inspired propulsion, underwater navigation, and environmental monitoring.

# Bibliography


[1] M. S. Triantafyllou, G. S. Triantafyllou, and D. K. P. Yue, “Hydrodynamics of fishlike swimming,” *Annu Rev Fluid Mech*, vol. 32, no. 1, pp. 33–53, 2000.

[2] M. Sfakiotakis, D. M. Lane, and J. B. C. Davies, “Review of fish swimming modes for aquatic locomotion,” *IEEE Journal of oceanic engineering*, vol. 24, no. 2, pp. 237–252, 1999.

[3] M. S. U. Khalid, J. Wang, H. Dong, and M. Liu, “Flow transitions and mapping for undulating swimmers,” *Phys Rev Fluids*, vol. 5, no. 6, p. 63104, 2020.

[4] D. Zhang, Q.-G. Huang, G. Pan, L.-M. Yang, and W.-X. Huang, “Vortex dynamics and hydrodynamic performance enhancement mechanism in batoid fish oscillatory swimming,” *J Fluid Mech*, vol. 930, p. A28, 2022.

[5] M. S. U. Khalid, J. Wang, I. Akhtar, H. Dong, M. Liu, and A. Hemmati, “Larger wavelengths suit hydrodynamics of carangiform swimmers,” *Phys Rev Fluids*, vol. 6, no. 7, p. 73101, 2021.

[6] E. J. Anderson, W. R. Mcgillis, and M. A. Grosenbaugh, “The boundary layer of swimming fish,” *Journal of Experimental Biology*, vol. 204, no. 1, pp. 81–102, 2001.

[7] M. S. U. Khalid, J. Wang, I. Akhtar, H. Dong, M. Liu, and A. Hemmati, “Why do anguilliform swimmers perform undulation with wavelengths shorter than their bodylengths?,” *Physics of Fluids*, vol. 33, no. 3, 2021.

[8] S. Gupta, A. Agrawal, K. Hourigan, M. C. Thompson, and A. Sharma, “Anguilliform and carangiform fish-inspired hydrodynamic study for an undulating hydrofoil: Effect of shape and adaptive kinematics,” *Phys Rev Fluids*, vol. 7, no. 9, p. 94102, 2022.

[9] Fe. Fish and G. V Lauder, “Passive and active flow control by swimming fishes and mammals,” *Annu. Rev. Fluid Mech.*, vol. 38, no. 1, pp. 193–224, 2006.

[10] F. E. Fish and G. V Lauder, “Control surfaces of aquatic vertebrates: active and passive design and function,” *Journal of Experimental Biology*, vol. 220, no. 23, pp. 4351–4363, 2017.

[11] G. V Lauder, “Fish locomotion: recent advances and new directions,” *Ann Rev Mar Sci*, vol. 7, no. 1, pp. 521–545, 2015.

[12] F. E. Fish, “Bio-inspired aquatic drones: Overview,” *Bioinspir Biomim*, no. 6, p. 60401, 2020.

[13] D. Zhang, J.-D. Zhang, and W.-X. Huang, “Physical models and vortex dynamics of swimming and flying: a review,” *Acta Mech*, vol. 233, no. 4, pp. 1249–1288, 2022.

[14] A. Raj and A. Thakur, “Fish-inspired robots: design, sensing, actuation, and autonomy—a review of research,” *Bioinspir Biomim*, vol. 11, no. 3, p. 31001, 2016.

[15] J. Montgomery, H. Bleckmann, and S. Coombs, “Sensory ecology and neuroethology of the lateral line,” *The lateral line system*, pp. 121–150, 2014.

[16] H. Bleckmann, J. Mogdans, and G. Dehnhardt, “Lateral line research: the importance of using natural stimuli in studies of sensory systems,” in *Ecology of sensing*, 2001, pp. 149–167.

[17] P. Domenici, J. M. Blagburn, and J. P. Bacon, “Animal escapology I: theoretical issues and emerging trends in escape trajectories,” *Journal of Experimental Biology*, vol. 214, no. 15, pp. 2463–2473, 2011.

[18] T. Bunnell, K. Hanisch, J. D. Hardege, and T. Breithaupt, “The fecal odor of sick hedgehogs (Erinaceus europaeus) mediates olfactory attraction of the tick Ixodes hexagonus,” *J Chem Ecol*, vol. 37, pp. 340–347, 2011.

[19] F. Ladich, “Peripheral hearing structures in fishes: diversity and sensitivity of catfishes and cichlids,” *Fish Hearing and Bioacoustics: An Anthology in Honor of Arthur N. Popper and Richard R. Fay*, pp. 321–340, 2016.

[20] H. Bleckmann and J. Mogdans, “Central processing of lateral line information,” *The lateral line system*, pp. 253–280, 2014.

[21] J. P. L. Cox, “Hydrodynamic aspects of fish olfaction,” *J R Soc Interface*, vol. 5, no. 23, pp. 575–593, 2008.

[22] C. Brönmark and L.-A. Hansson, “Aquatic chemical ecology: new directions and challenges for the future,” *Chemical ecology in aquatic systems*, pp. 272–278, 2012.

[23] J. Hemmer-Hansen *et al.*, “Genetic analyses reveal complex dynamics within a marine fish management area,” *Evol Appl*, vol. 12, no. 4, pp. 830–844, 2019.

[24] P. W. Webb, “Control of posture, depth, and swimming trajectories of fishes,” *Integr Comp Biol*, vol. 42, no. 1, pp. 94–101, 2002.

[25] A. Menzer, M. Lei, C. Li, and H. Dong, “A Multiphysics Approach to Understanding Chemoreception in Bio-Robotic Fish Schools,” in *ASME International Mechanical Engineering Congress and Exposition*, 2023, p. V009T10A070.

[26] C. Li, H. Dong, and K. Zhao, “A balance between aerodynamic and olfactory performance during flight in Drosophila,” *Nat Commun*, vol. 9, no. 1, p. 3215, 2018.

[27] M. Lei and C. Li, “Wings and whiffs: Understanding the role of aerodynamics in odor-guided flapping flight,” *Physics of Fluids*, vol. 35, no. 12, 2023.

[28] R. T. Cardé, “Navigation along windborne plumes of pheromone and resource-linked odors,” *Annu Rev Entomol*, vol. 66, no. 1, pp. 317–336, 2021.

[29] H. Farooq, I. Akhtar, A. Hemmati, and M. S. U. Khalid, “An Accurate Immersed Boundary Method Using Radial-Basis Functions for Incompressible Flows,” *Under Review, Available at SSRN 4874977*, 2024.

[30] C. Kim *et al.*, “Artificial olfactory sensor technology that mimics the olfactory mechanism: A comprehensive review,” *Biomater Res*, vol. 26, no. 1, p. 40, 2022.

[31] G. Bianchi, S. Cinquemani, and F. Resta, “Bio-inspired design of an underwater robot exploiting fin undulation propulsion,” *Applied Sciences*, vol. 11, no. 6, p. 2556, 2021.

[32] S. Marras and M. Porfiri, “Fish and robots swimming together: attraction towards the robot demands biomimetic locomotion,” *J R Soc Interface*, vol. 9, no. 73, pp. 1856–1868, 2012.

[33] J. Sinha, K. B. Lua, and S. M. Dash, “Influence of the pivot location on the thrust and propulsive efficiency performance of a two-dimensional flapping elliptic airfoil in a forward flight,” *Physics of Fluids*, vol. 33, no. 8, 2021.

[34] J. Sinha, S. M. Dash, and K. B. Lua, “On the study of the pitch angular offset effects at various flapping frequencies for a two-dimensional asymmetric flapping airfoil in forward flight,” *Physics of Fluids*, vol. 36, no. 4, 2024.

[35] K. N. Lucas, G. V Lauder, and E. D. Tytell, “Airfoil-like mechanics generate thrust on the anterior body of swimming fishes,” *Proceedings of the National Academy of Sciences*, vol. 117, no. 19, pp. 10585–10592, 2020.

[36] B. J. Gemmell, S. P. Colin, J. H. Costello, and J. O. Dabiri, “Suction-based propulsion as a basis for efficient animal swimming,” *Nat Commun*, vol. 6, no. 1, p. 8790, 2015.

[37] S.-J. Hsu, H. Deng, J. Wang, H. Dong, and B. Cheng, “Wing deformation improves aerodynamic performance of forward flight of bluebottle flies flying in a flight mill,” *J R Soc Interface*, vol. 21, no. 216, p. 20240076, 2024.

[38] Z. Huang, A. Menzer, J. Guo, and H. Dong, “Hydrodynamic analysis of fin–fin interactions in two-manta-ray schooling in the vertical plane,” *Bioinspir Biomim*, vol. 19, no. 2, p. 26004, 2024.

[39] H. Liu, R. Wassersug, and K. Kawachi, “The three-dimensional hydrodynamics of tadpole locomotion,” *Journal of Experimental Biology*, vol. 200, no. 22, pp. 2807–2819, 1997.

[40] M. Gazzola, W. M. Van Rees, and P. Koumoutsakos, “C-start: optimal start of larval fish,” *J Fluid Mech*, vol. 698, pp. 5–18, 2012.

[41] A. N. Zurman-Nasution, B. Ganapathisubramani, and G. D. Weymouth, “Influence of three-dimensionality on propulsive flapping,” *J Fluid Mech*, vol. 886, p. A25, 2020.

[42] M. Gazzola, M. Argentina, and L. Mahadevan, “Scaling macroscopic aquatic locomotion,” *Nat Phys*, vol. 10, no. 10, pp. 758–761, 2014.

[43] U. K. Muller, J. G. M. van den Boogaart, and J. L. van Leeuwen, “Flow patterns of larval fish: undulatory swimming in the intermediate flow regime,” *Journal of Experimental Biology*, vol. 211, no. 2, pp. 196–205, 2008.

[44] G. V Lauder and E. D. Tytell, “Hydrodynamics of undulatory propulsion,” *Fish physiology*, vol. 23, pp. 425–468, 2005.

[45] M. S. U. Khalid, I. Akhtar, and H. Dong, “Hydrodynamics of a tandem fish school with asynchronous undulation of individuals,” *J Fluids Struct*, vol. 66, pp. 19–35, 2016.

[46] J. J. Videler, *Fish swimming*, vol. 10. Springer Science & Business Media, 1993.

[47] A. P. Maertens, A. Gao, and M. S. Triantafyllou, “Optimal undulatory swimming for a single fish-like body and for a pair of interacting swimmers,” *J Fluid Mech*, vol. 813, pp. 301–345, 2017.

[48] R. Mittal, H. Dong, M. Bozkurttas, F. M. Najjar, A. Vargas, and A. Von Loebbecke, “A versatile sharp interface immersed boundary method for incompressible flows with complex boundaries,” *J Comput Phys*, vol. 227, no. 10, pp. 4825–4852, 2008.

[49] M. Kamran, A. Fardi, C. Li, and M. S. U. Khalid, “How does vortex dynamics help undulating bodies spread odor?,” *Physics of Fluids*, vol. 36, no. 11, 2024.

[50] M. Lei, J. P. Crimaldi, and C. Li, “Navigation in odor plumes: How do the flapping kinematics modulate the odor landscape?,” in *AIAA Aviation 2021 Forum*, 2021, p. 2817.

[51] Y. Y. Yan and Y. Q. Zu, “Numerical simulation of heat transfer and fluid flow past a rotating isothermal cylinder–a LBM approach,” *Int J Heat Mass Transf*, vol. 51, no. 9–10, pp. 2519–2536, 2008.

[52] M. Lei, M. A. Willis, B. E. Schmidt, and C. Li, “Numerical Investigation of Odor-Guided Navigation in Flying Insects: Impact of Turbulence, Wingbeat-Induced Flow, and Schmidt Number on Odor Plume Structures,” *Biomimetics*, vol. 8, no. 8, p. 593, 2023.

[53] G. Liu, Y. Ren, H. Dong, O. Akanyeti, J. C. Liao, and G. V Lauder, “Computational analysis of vortex dynamics and performance enhancement due to body–fin and fin–fin interactions in fish-like locomotion,” *J Fluid Mech*, vol. 829, pp. 65–88, 2017, doi: 10.1017/jfm.2017.533.

[54] J. C. R. Hunt, A. A. Wray, and P. Moin, “Eddies, streams, and convergence zones in turbulent flows,” *Studying turbulence using numerical simulation databases, 2. Proceedings of the 1988 summer program*, 1988.